Cell Reports

Article

An atypical GABARAP binding module drives the pro-autophagic potential of the AML-associated NPM1c variant

Graphical abstract

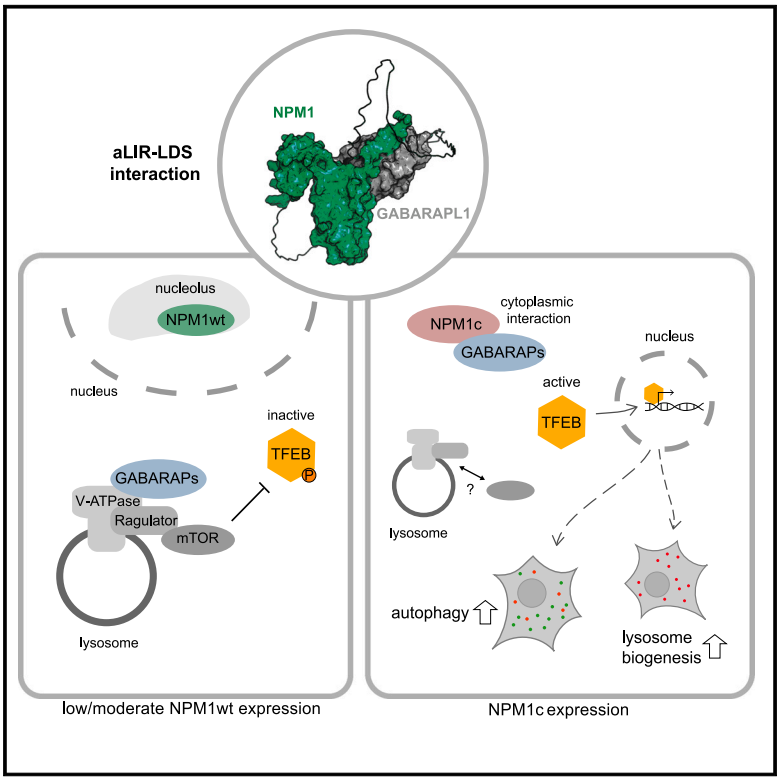

Highlights

- NPM1/NPM1c induce the autophagy-lysosome pathway by activating the master regulator TFEB
- NPM1/NPM1c bind to GABARAP proteins via an atypical module in their N-terminal regions
- The pro-autophagic activity of NPM1c depends on this GABARAP binding module

Authors

Hannah Mende, Anshu Khatri, Carolin Lange, ..., Vladimir V. Rogov, Ramachandra M. Bhaskara, Stefan Müller

Correspondence

bhaskara@med.uni-frankfurt.de (R.M.B.), ste.mueller@em.uni-frankfurt.de (S.M.)

In brief

Mende and co-workers report that NPM1 and NPM1c induce the autophagy-lysosome pathway by activating the master transcription factor TFEB. They identify an atypical GABARAP binding module in the N-terminal region of NPM1 and the AML-associated oncogenic mutant NPM1c and show that the pro-autophagic activity of NPM1c depends on this module.

Mende et al., 2023, Cell Reports *42*, 113484
December 26, 2023
https://doi.org/10.1016/j.celrep.2023.113484

CellPress

Cell Reports

CellPress
OPEN ACCESS

Article

An atypical GABARAP binding module drives the pro-autophagic potential of the AML-associated NPM1c variant

Hannah Mende,[1] Anshu Khatri,[2] Carolin Lange,[1,3] Sergio Alejandro Poveda-Cuevas,[1,3] Georg Tascher,[1] Adriana Covarrubias-Pinto,[1] Frank Löhr,[2] Sebastian E. Koschade,[1,6] Ivan Dikic,[1] Christian Münch,[1] Anja Bremm,[1] Lorenzo Brunetti,[7] Christian H. Brandts,[6] Hannah Uckelmann,[8] Volker Dötsch,[2] Vladimir V. Rogov,[4,5] Ramachandra M. Bhaskara,[1,3,*] and Stefan Müller[1,9,*]

[1]Goethe University Frankfurt, Institute of Biochemistry II, Theodor-Stern-Kai 7, 60590 Frankfurt, Germany
[2]Goethe University Frankfurt, Institute of Biophysical Chemistry and Center for Biomolecular Magnetic Resonance, Max-von-Laue Street 9, 60438 Frankfurt, Germany
[3]Goethe University Frankfurt, Buchmann Institute for Molecular Life Sciences, Max-von-Laue Street 15, 60438 Frankfurt, Germany
[4]Goethe University Frankfurt, Institute of Pharmaceutical Chemistry, Max-von-Laue Street 15, 60438 Frankfurt, Germany
[5]Goethe University Frankfurt, Structural Genomics Consortium, Buchmann Institute for Molecular Life Sciences, Max-von-Laue Street 15, 60438 Frankfurt, Germany
[6]Goethe University Frankfurt, University Hospital, Department of Medicine, Hematology/Oncology, Theodor-Stern-Kai 7, 60590 Frankfurt, Germany
[7]Marche Polytechnic University, Department of Clinical and Molecular Sciences, Via Tronto 10, 60020 Ancona, Italy
[8]Goethe University Frankfurt, University Hospital, Department of Pediatrics, Theodor-Stern-Kai 7, 60590 Frankfurt, Germany
[9]Lead contact
*Correspondence: bhaskara@med.uni-frankfurt.de (R.M.B.), ste.mueller@em.uni-frankfurt.de (S.M.)
https://doi.org/10.1016/j.celrep.2023.113484

SUMMARY

The nucleolar scaffold protein NPM1 is a multifunctional regulator of cellular homeostasis, genome integrity, and stress response. NPM1 mutations, known as NPM1c variants promoting its aberrant cytoplasmic localization, are the most frequent genetic alterations in acute myeloid leukemia (AML). A hallmark of AML cells is their dependency on elevated autophagic flux. Here, we show that NPM1 and NPM1c induce the autophagy-lysosome pathway by activating the master transcription factor TFEB, thereby coordinating the expression of lysosomal proteins and autophagy regulators. Importantly, both NPM1 and NPM1c bind to autophagy modifiers of the GABARAP subfamily through an atypical binding module preserved within its N terminus. The propensity of NPM1c to induce autophagy depends on this module, likely indicating that NPM1c exerts its pro-autophagic activity by direct engagement with GABARAPL1. Our data report a non-canonical binding mode of GABARAP family members that drives the pro-autophagic potential of NPM1c, potentially enabling therapeutic options.

INTRODUCTION

Autophagy is a process by which cytoplasmic content, such as proteins, nucleic acids, or organelles, is engulfed by autophagosomes and delivered for lysosomal degradation.[1,2] Initiated by the formation of phagophores, the closed double-membrane-coated autophagosomes subsequently fuse with lysosomes, where the designated cargo is degraded. Autophagy serves multiple cellular purposes, including the clearance of damaged organelles or protein aggregates. By providing building blocks and energy, autophagy plays a vital role in sustaining cell survival upon starvation.[1–3] The mechanistic target of rapamycin (mTOR) kinase complex controls starvation-induced autophagy. In fed cells, mTOR allows cell growth and synthesis of new proteins, actively repressing macroautophagy via phosphorylation of Unc-51-like autophagy activating kinase (ULK1), which is required to initiate phagophore formation.[4,5] The regulated activity of these upstream kinases is necessary to control the synchronized action of several autophagy-related (ATG) proteins.

A key step in both autophagosome formation and autophagosome-lysosome fusion is the conjugation of human ATG8 (hATG8) family proteins to specific lipids in autophagosomal membranes by a ubiquitin-like conjugation pathway.[6] Lipidated ATG8s act as adaptors to recruit a variety of proteins, such as cargo components, receptors, and factors modulating the phagophore. The hATG8 family is composed of the LC3 (MAP1LC3A, MAP1LC3B, MAP1LC3C) and the GABARAP (GABARAP, GABARAPL1, GABARAPL2) subfamilies.[7] LC3 proteins appear to be more important for recruiting cargo to the phagophores, while GABARAPs play critical roles in autophagosome assembly as well as autophagosome-lysosome fusion.[8] GABARAPs are instrumental in coordinating the autophagosomal pathway with

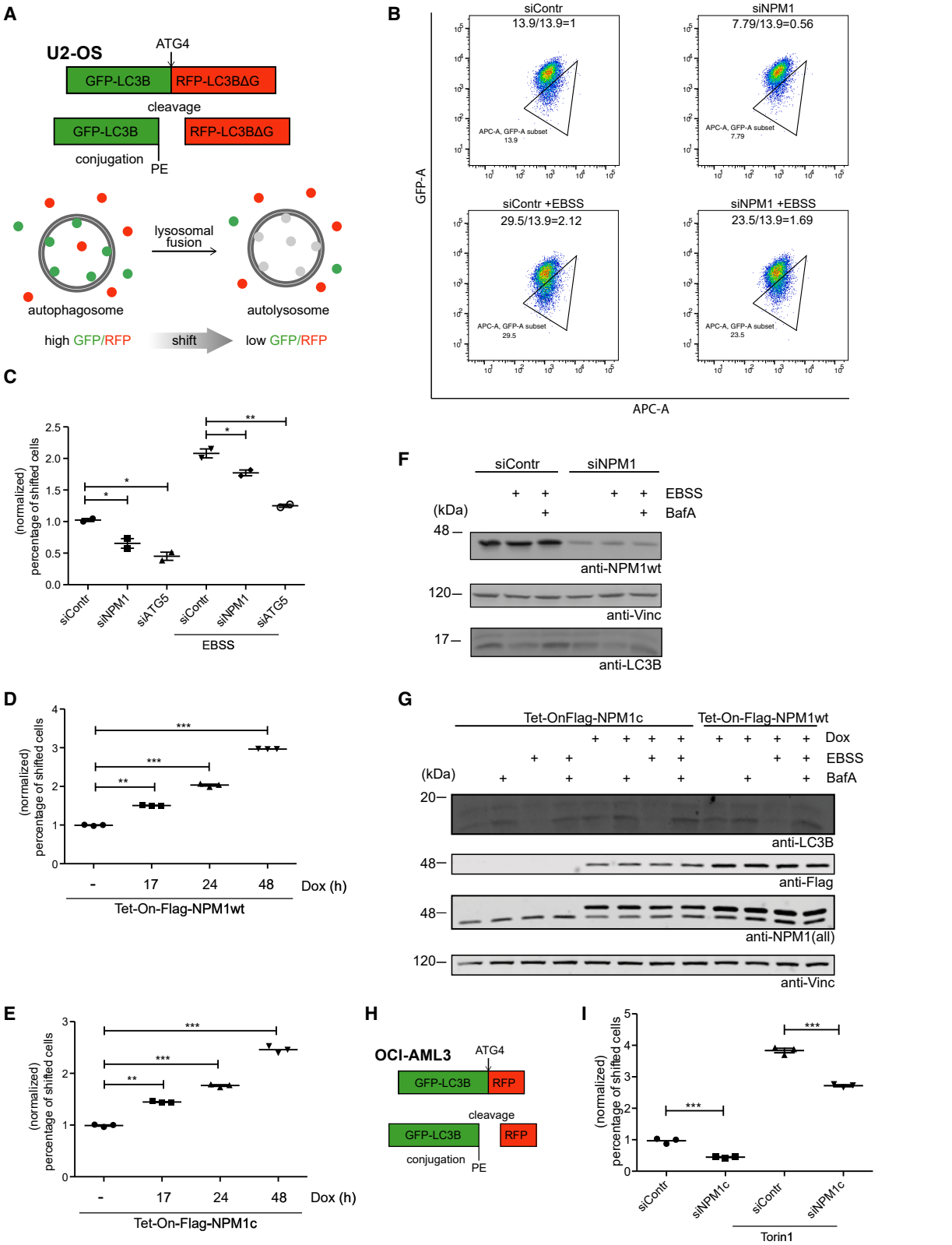

(legend on next page)

lysosomal biogenesis by controlling the activity of the transcription factor EB (TFEB), a key transcriptional activator of the lysosomal system.[9,10]

The function of both ATG8 subfamilies (LC3 and GABARAP proteins) primarily relies on their ability to mediate distinct protein-protein interactions by binding to specific sequence motifs.[11] Best described are the LC3-interacting regions (LIRs), or ATG8 interacting motifs, which bind to a hydrophobic patch of hATG8s, the so-called LIR docking site (LDS). LIRs generally reside in unstructured regions of a protein and bind to the LDS of ATG8 proteins by augmenting an inter-molecular β sheet. Canonical LIRs are characterized by a hydrophobic core sequence motif [W/F/Y]-X_1-X_2-[L/V/I], in which the conserved aromatic residues and the apolar residues fit into the two surface hydrophobic pockets (HP1 and HP2) of the LDS.[12,13] Acidic residues or phosphorylated serine/threonine residues adjacent to the core LIR motif further stabilize the binding by interacting with the positively charged surface surrounding the LDS.[14,15] Non-canonical or atypical LIRs (aLIRs) lack the characteristic aromatic residue(s) of a LIR.[16,17] In addition to the LIR-LDS interaction, ATG8s can use other interaction surfaces, such as the ubiquitin-interacting motif docking site (UDS), which resides on the opposite face of ATG8 proteins.

Alterations in autophagic pathways are linked to human diseases, including neurodegeneration and cancer.[18,19] For instance, in acute myeloid leukemia (AML) deregulation of autophagy in hematopoietic stem cells contributes to leukemogenesis.[20] In addition, the upregulation of autophagy represents a resistance mechanism.[21] However, the role of autophagy might be different depending on the leukemic cell populations, such as leukemic stem cells or progenitor cells.[22] The most frequent genetic alterations in AML are mutations of nucleophosmin (NPM1).[23]

NPM1 regulates critical cellular processes, including ribosome biogenesis, centrosome duplication, cell proliferation, and survival. It is a predominantly nucleolar protein that shuttles between the nucleolus/nucleoplasm and the cytoplasm.[24] Interestingly, NPM1 plays a dosage-dependent dual role as a tumor suppressor and oncoprotein.[25] The overexpression of NPM1 in solid human tumors correlates with increased cell growth and proliferation. In AML, NPM1 mutations are found in about 50% of cases with a normal karyotype.[26] In almost all cases, the mutations are found in exon 12, and the most frequent mutation (type A) is a tetranucleotide duplication.[27] These mutations alter the extreme C terminus of NPM1, generating a nuclear export signal, which is recognized by the chromosomal maintenance 1 (CRM1, also known as Exportin1 or XPO1) export factor. Consequently, these NPM1 variants (NPM1c), are delocalized from the nucleolus/nucleoplasm to the cytosol. Despite this defined molecular alteration, the role of NPM1c in mediating tumorigenesis is not fully understood.

Here, we show that NPM1 and NPM1c harbor an atypical LIR (aLIR) at the N terminus that mediates their interaction with the GABARAP subfamily of hATG8 proteins. We further demonstrate that the interaction of NPM1c with GABARAP family proteins triggers its pro-autophagic activity through the activation of TFEB, which in turn functions as the master transcription regulator of the autophagy-lysosomal pathway. Our data reveal a signaling mode that connects the AML-associated NPM1c variant to autolysosomal biogenesis.

RESULTS

NPM1 controls the autophagic flux

To monitor the impact of NPM1 on the autophagic flux, we used the fluorescence-based GFP-LC3B-RFP-LC3BΔG reporter system (Figure 1A).[28] Upon cleavage by ATG4 proteases, this probe generates GFP-LC3B and RFP-LC3BΔG. During autophagosome formation, GFP-LC3B is conjugated to autophagosomal membranes and gets subsequently degraded, while RFP-LC3BΔG serves as a stable internal control. Thus, the shift of cells into the autophagy-positive gate with a decreased GFP/RFP ratio, measured by flow cytometry, is indicative of the autophagic flux. As a control, the autophagic regulator ATG5 was depleted by siRNA reducing the autophagic flux under both basal conditions and upon amino acid starvation (Figures 1B and 1C). Importantly, the depletion of NPM1 also leads to a significant reduction of basal or starvation-induced autophagic flux, suggesting a pro-autophagic role for NPM1 (Figures 1B and 1C). In line with this, overexpression of NPM1

Figure 1. NPM1 and NPM1c are involved in autophagic flux modulation

(A) Scheme of the U-2 $OS^{GFP\text{-}LC3B\text{-}RFP\text{-}LC3B\Delta G}$ reporter cell line to monitor autophagic flux. Green and red fluorescence is measured by flow cytometry, and autophagy-positive cells are quantified by the percentage of cells shifting into a gate with a low GFP/RFP ratio.

(B) Representative dot blots from flow cytometric analysis of the U-2 $OS^{GFP\text{-}LC3B\text{-}RFP\text{-}LC3B\Delta G}$ reporter cell line. Cells were transfected with siRNA targeting NPM1 or a non-human target control for 72 h and starved with EBSS treatment for 4 h before analysis when indicated. The triangle gates the APC-A, GFP-A subset of autophagy-positive cells. Calculations show the normalization of the percentage of cells in the autophagy-positive gate to the control.

(C) Quantification of flow cytometric analysis of U-2 $OS^{GFP\text{-}LC3B\text{-}RFP\text{-}LC3B\Delta G}$ cells transfected with siRNA as indicated. When indicated, cells were starved with EBSS treatment for 4 h before analysis. Data are presented as mean ± SD of the normalized percentage of cells in the autophagy-positive gate. n = 2, *$p < 0.05$, **$p < 0.01$, as analyzed by one-way ANOVA followed by Tukey's multiple comparison test.

(D and E) Quantification of flow cytometric analysis of U-2 $OS^{GFP\text{-}LC3B\text{-}RFP\text{-}LC3B\Delta G}$ with Tet-inducible Flag-NPM1 (D) or Flag-NPM1c (E), treated with doxycycline (0.1 μg/mL) for the indicated time points. Data are presented as mean ± SD of the normalized percentage of cells in the autophagy-positive gate, n = 3 biological replicates, ***$p < 0.001$, as analyzed by one-way ANOVA followed by Tukey's multiple comparison test.

(F) Immunoblot of U-2 OS cells transfected with NPM1 siRNA or control siRNA for 72 h and treated with EBSS and 200 nM bafilomycin A for 4 h as indicated.

(G) Immunoblot of U-2 OS cells with Tet-inducible Flag-NPM1 or Flag-NPM1c treated with doxycycline for 24 h to induce the expression of Flag-NPM1 and Flag-NPM1c in combination with EBSS and 200 nM bafilomycin A for 4 h as indicated.

(H) Scheme of the OCI-$AML3^{GFP\text{-}LC3B\text{-}RFP}$ reporter cell line to monitor autophagic flux, as shown in (A).

(I) Quantification of flow cytometric analysis of OCI-$AML3^{GFP\text{-}LC3B\text{-}RFP}$ cells transfected with siRNA targeting NPM1c or a non-human target control for 72 h. When indicated, cells are additionally treated with 150 nM Torin 1 for 4 h before analysis. Data are presented as mean ± SD of the normalized percentage of cells in the autophagy-positive gate. n = 3, ***$p < 0.001$, as analyzed by one-way ANOVA followed by Tukey's multiple comparison test.

from a doxycycline-inducible vector system increased the autophagic flux (Figures 1D and S1A). Notably, this increase correlates with the duration and the levels of NPM1 expression. Importantly, the autophagic flux is also strongly induced upon expression of the AML-associated NPM1c mutant (Figures 1E and S1A). Given that NPM1c generally exhibits lower expression levels than wild-type NPM1 due to enhanced proteasomal degradation[29] (Figures S1A and S1H), this strongly supports a potent pro-autophagic potential of NPM1c. The findings obtained with the flux reporter were confirmed by anti-LC3B immunoblotting revealing a reduced lipidation of LC3B upon depletion of NPM1 and enhanced lipidation upon overexpression of either NPM1 or NPM1c in U-2 OS cells (Figures 1F and 1G).

To validate these findings, we used the GFP-mCherry-LC3B reporter for microscopy-based autophagic flux measurement (Figure S1B).[30] This reporter system relies on the reduced GFP fluorescence relative to mCherry in the acidic environment of the autolysosome. Thus, the ratio of mCherry-positive dots, representing autophagosomes and lysosomes, versus mCherry and GFP co-localizing dots, only representing autophagosomes, serves as a readout for autophagic flux. Depletion of NPM1 by siRNA reduces this ratio (Figure S1C), whereas expression of either NPM1 or NPM1c shifts the ratio toward mCherry-positive dots (Figures S1D–S1F). To investigate whether NPM1 or NPM1c might be targeted to autophagosomes for degradation, we followed their protein levels in the presence of the translation inhibitor cycloheximide. Notably, protein levels of Flag-NPM1 and Flag-NPM1c during starvation remain stable upon addition of the lysosomal inhibitor bafilomycin A1, indicating that NPM1 and NPM1c are unlikely autophagic cargo or function as autophagy receptors (Figures S1G and S1H).

To further explore the impact of NPM1c on autophagy in AML cells, we used an NPM1c-positive OCI-AML3 cell line expressing GFP-LC3B-RFP, a modified version of the autophagic flux reporter of Figure 1A (Figure 1H).[22,28] Flow cytometry analysis upon NPM1c depletion, using a specific siRNA that does not affect the protein levels of wild-type NPM1, leads to a reduction of autophagic flux under basal conditions and autophagy stimulation upon mTOR inhibition by Torin 1 treatment (Figures 1I and S1I).

Notably, depletion of wild-type NPM1 in NPM1c-negative AML cell lines, such as Hel276 and MV4-11, does not impact the autophagic flux indicating a more pronounced role of NPM1c in the control of autophagy in AML cells (Figures S1J–S1L). As the role of NPM1 as a tumor suppressor or oncogene depends on the expression level in the respective cell type, we anticipate that the autophagic flux is also affected in a cell-type-specific manner.

Altogether, these data demonstrate that NPM1 and, in particular, the AML-associated NPM1c variant, act as modulators of autophagic flux.

NPM1 and the AML-associated NPM1c variant bind to GABARAP family members

Numerous proteins involved in autophagy bind to hATG8 proteins to exert their functions. To test whether NPM1 binds to hATG8 family members, GST-tagged LC3B, GABARAP, GABARAPL1, and GABARAPL2 were used as affinity baits in HEK293 cell lysates expressing Flag-tagged NPM1. Compared with GST or GST-LC3B, all GST-tagged GABARAP family members strongly enrich Flag-NPM1 from cell extracts (Figure 2A). To explore whether the association of NPM1 and GABARAPL1 is due to a direct physical interaction, GST-tagged NPM1 and His-tagged GABARAPL1 expressed and purified from bacteria were incubated in the absence or presence of cell lysate. His-GABARAPL1 is retained on glutathione Sepharose-bound GST-NPM1 irrespective of the addition of cell lysate, indicating that both proteins interact directly (Figure 2B).

Notably, GST pull-down experiments with lysates from HEK293 cells expressing Flag-tagged NPM1 or the AML-associated NPM1c variant show binding to GST-tagged GABARAPL1 to a similar extent (Figure 2C). To validate the relevance of these interactions under endogenous expression levels in AML cells, we performed GST pull-down experiments with extracts from OCI-AML2 (wild-type NPM1) and OCI-AML3 (heterozygous for NPM1c). Consistent with results from ectopically expressed NPM1 and NPM1c, wild-type NPM1 from both OCI-AML2 and OCI-AML3 lysates was captured on GST-GABARAPL1 beads, while NPM1c was specifically bound from lysates of OCI-AML3 cells (Figure 2D).

To investigate where Flag-NPM1 or Flag-NPM1c associate with GABARAP proteins *in situ*, we performed proximity ligation assays (PLA) (Figures 2E, 2F, and S2A–S2D). Wild-type NPM1 co-localized with endogenous GABARAP family members in the nucleoplasm and, to a lesser extent, in the cytoplasm. By contrast, the largely cytoplasmic NPM1c variant exhibits a more prominent co-localization with GABARAPs in the cytosol. The comparison of total PLA-positive signals per cell reveals a stronger association of NPM1c with GABARAPs than wild-type NPM1 despite lower protein levels (Figures 2F and S2B). Notably, these interactions are not affected by the accumulation of autolysosomes upon bafilomycin A1 treatment. While staining of GABARAPs reveals characteristic cytoplasmic foci of autophagosomes, PLA signals with Flag-NPM1 and Flag-NPM1c are relatively independent of these structures. This indicates that NPM1 and NPM1c interact primarily with the non-conjugated pool of GABARAP proteins.

NPM1 and NPM1c control autolysosome biogenesis through the activation of TFEB

To investigate how NPM1 affects GABARAP functions, we compared the interactome of HA-GABARAPL1 in control cells and cells depleted from NPM1 by siRNA (Figure 3A). In anti-HA immunoprecipitations from HA-GABARAPL1-expressing control cells, around 1,108 proteins were enriched ($\geq$1.5-fold) over mock-transfected cells (Table S1). These include well-known interactors of GABARAPL1, such as components of the ATG core machinery (ATG3, ATG4B, ATG7, or ATG13) (Figures S3A–S3D).[31] Intriguingly, a comparison of GABARAPL1-associated proteins from NPM1-depleted cells and control cells reveals a strong enrichment of lysosomal membrane proteins, including subunits of the vacuolar-type ATPase (V-ATPase) (Figures 3B and 3C) upon loss of NPM1. The lysosomal V-ATPase-Ragulator complex controls TFEB activity via mTOR-dependent phosphorylation, depending on the amino acid content within the lysosomal lumen (Figure 3D).[32] Several lines of evidence

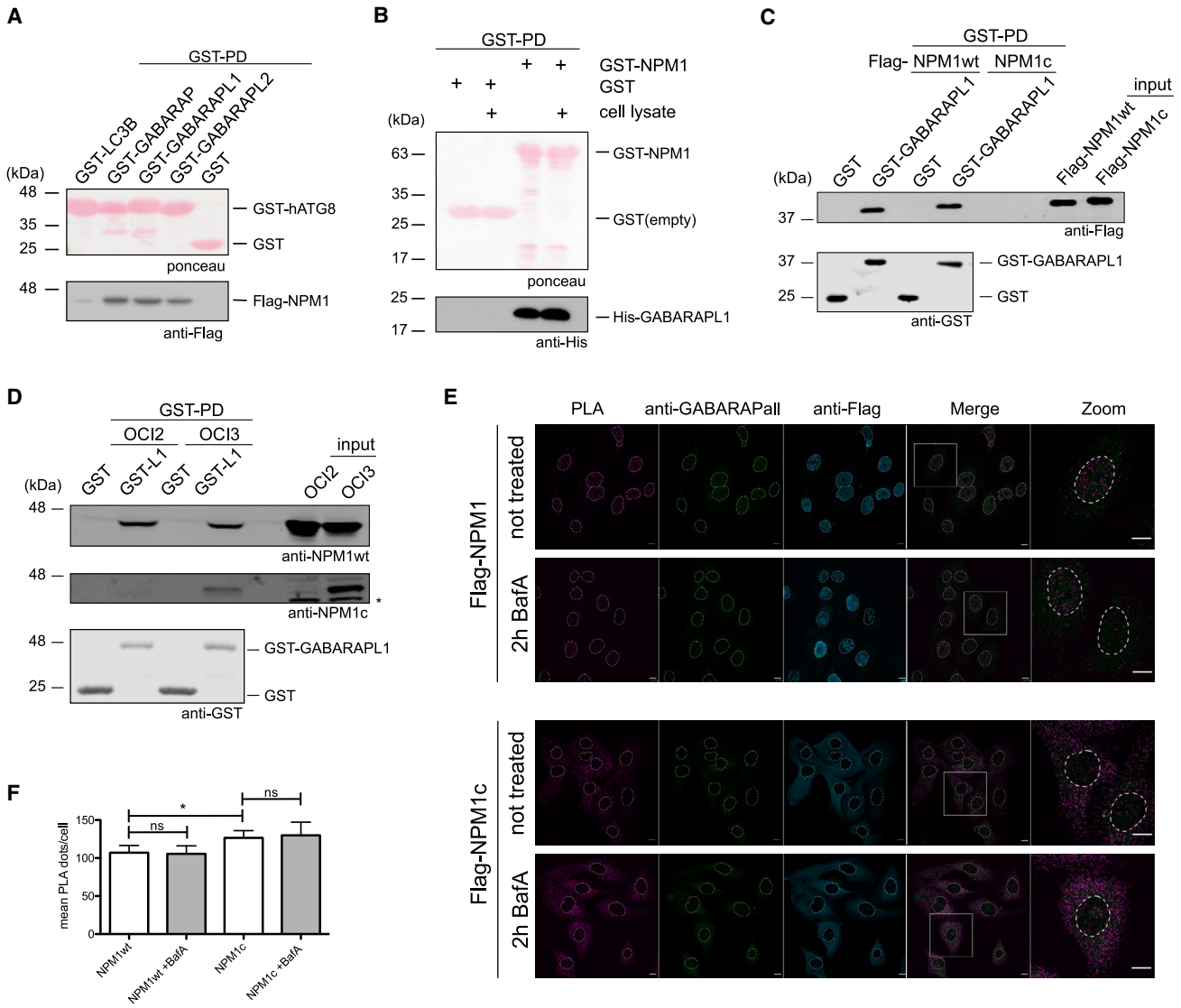

Figure 2. NPM1 and NPM1c directly interact with the GABARAP protein family

(A) Immunoblot of a GST pull-down with immobilized GST empty, GST-LC3B, and GST-GABARAPs with HEK cell lysate expressing Flag-NPM1.

(B) Immunoblot of an *in vitro* interaction assay with immobilized empty GST and GST-NPM1 incubated with purified His-GABARAPL1 protein in the absence or presence of cell lysate.

(C) Immunoblot of a GST pull-down with immobilized GST-GABARAPL1 with HEK cell lysate expressing Flag-NPM1 and Flag-NPM1c.

(D) Immunoblot of a GST pull-down with immobilized GST-GABARAPL1 with NPM1wt OCI-AML2 (OCI2) and heterozygous NPM1wt/c OCI-AML3 (OCI3) cell lysate. *Unspecific band.

(E) Representative images of a proximity ligation assay (PLA) of U-2 OS cells expressing Flag-NPM1 and Flag-NPM1c under a Tet-inducible promotor using antibodies for Flag and all endogenous GABARAPs. If stated, cells were treated with 200 nm bafilomycin A1 (BafA) for 2 h. Nuclei are shown as dotted lines. Scale bar, 10 μm.

(F) Quantification of the PLA assay from (E). If stated, cells were treated with 200 nM BafA for 2 h. Data are presented as mean ± SD, n = 4, *p < 0.05, as analyzed by a two-sided t test. At least 140 cells were counted per replicate.

indicate that GABARAP family members are necessary for the V-ATPase-dependent TFEB activation.[9,33]

Given the impact of NPM1 on the association of GABARAPL1 with components of the V-ATPase complex, we tested if decreased cellular NPM1 levels affect lysosome morphology by utilizing LysoTracker red staining (Figure 3E). We found that inhibition of mTOR activity triggers an increase in lysosome size, potentially due to autolysosomal fusion events or induced lysosome biogenesis. This effect is strongly limited upon NPM1 depletion, pointing to a role of NPM1 in lysosome homeostasis.

To directly explore the effects of NPM1 and NPM1c on autolysosome biology, we compared the proteomes of cells either expressing wild-type NPM1 or NPM1c to control cells (Figures 4A,

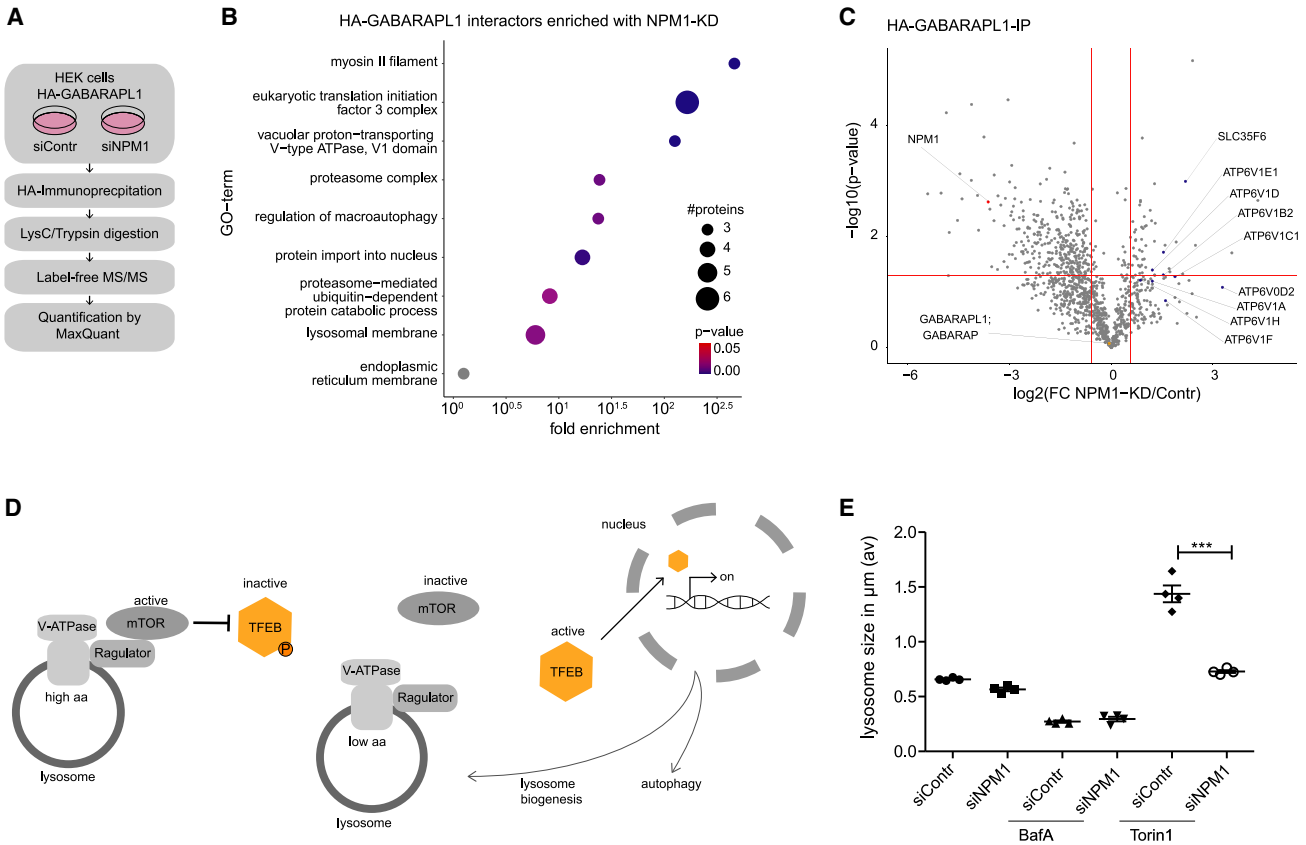

Figure 3. NPM1 depletion modulates GABARAPL1 interaction with lysosomal proteins

(A) Experimental setup of a quantitative HA-GABARAPL1 immunoprecipitation using mass spectrometry. HEK cells were transfected with siRNA against NPM1 or a non-human target (siContr) and transiently overexpress HA-GABARAPL1.

(B) Gene ontology (GO) term enrichment of HA-GABARAPL1 interactors with NPM1 KD compared with the control. Only proteins with a significant enrichment over the IP control ($p < 0.05$ [$-\log10 > 1.3$] and FC > 1.5 [log2 > 0.58]) in one of the conditions were used for analysis.

(C) Volcano plot of HA-GABARAPL1 immunoprecipitations comparing enriched proteins of the NPM1 with the control knockdown (KD). Proteins of the V-ATPase complex and the lysosomal membrane were highlighted. Only proteins with significant enrichment over the IP control in one of the conditions are depicted here. Red lines indicate significance intervals of $p < 0.05$ ($-\log10 > 1.3$) and FC > 1.5 (log2 > 0.58).

(D) Model of how TFEB activity is controlled by the interaction of the V-ATPase, Ragulator (LAMTOR1-5), and mTORC1 complexes on the lysosomal surface.

(E) Quantification of the average (av) area of the LysoTracker red staining indicative of the lysosomal size in U-2 OS cells transfected with siRNA targeting NPM1 or a non-human target control. If indicated, cells were treated with 100 nM BafA or 200 nM Torin 1 for 17 h. Data are presented as mean ± SD, n = 4 biological replicates, ***$p < 0.001$, as analyzed by one-way ANOVA followed by Tukey's multiple comparison test.

4B, and S4A–S4C; Table S2). Functional clustering of upregulated proteins upon expression of NPM1 and NPM1c reveals the enrichment of lysosomal and autophagosomal proteins (Figure 4B). Notably, despite its lower expression, NPM1c has a more pronounced impact than wild-type NPM1 on the number and extent of enriched/regulated autolysosomal proteins (Figures 4B and S4C). Strikingly, GABARAPL1 was identified in our dataset as one of the most strongly upregulated proteins upon expression of NPM1c. While it is tempting to conclude that NPM1c might stabilize GABARAPL1 on a protein level, RT-qPCR demonstrated that the increase in protein levels is accompanied by elevated mRNA levels of *GABARAPL1* (Figure S4D). To follow the idea that lysosomal and autophagosomal protein abundance is affected by NPM1c in AML cells, we performed a proteomics experiment in an OCI-AML3 cell engineered for targeted degradation of NPM1c with dTAG-13 treatment (OCI-AML3$^{NPM1c\text{-}FKBP12}$).[34] Degradation of NPM1c leads to the loss of proteins involved in transcription, specifically homeobox proteins, which has been extensively studied in the context of AML. Importantly, we also observed reduced levels of proteins associated with autophagy, underlining the impact of NPM1c on the expression of the autolysosomal machinery (Figure 4C; Table S3). Notably, these findings are also perfectly in line with a recently published RNA-seq dataset generated from a mouse HOXB8-ER-immortalized cell line, where a heterozygous knockin of human NPM1c induces mRNA abundance of lysosomal proteins.[35]

As autophagosomal and lysosomal proteins are known transcriptional targets of TFEB, these observations strengthen our finding that NPM1 modulates the interaction of GABARAPL1 with the lysosomal V-ATPase thereby activating the downstream regulator TFEB. We monitored whether NPM1 or NPM1c

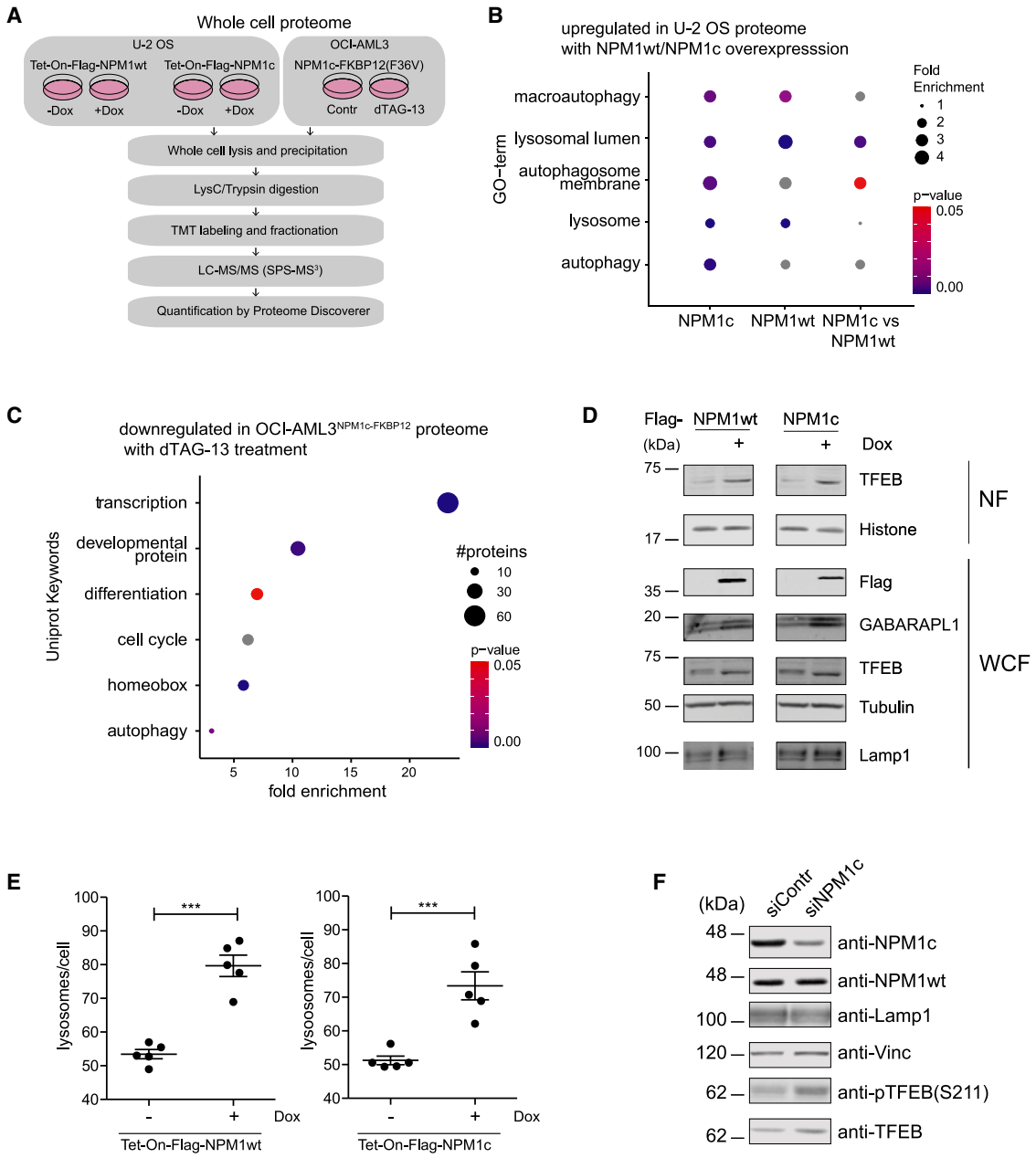

Figure 4. Moderate overexpression of NPM1c and high overexpression of NPM1 leads to transcriptional upregulation of GABARAPL1 together with TFEB nuclear translocation

(A) Experimental setup of a whole-cell proteome of U-2 OS cells with Tet-inducible Flag-NPM1 or Flag-NPM1c expression in (B) and of OCI-AML3 cells with endogenously tagged NPM1c-FKBP12(F36V) in (C) using tandem mass tag (TMT)-based mass spectrometry (MS). Expression of the transgene is induced for 24 h with 0.1 μg/mL doxycycline, and degradation of NPM1c-FKBP12(F36V) is induced by 500 nM dTAG-13 treatment for 24 h. SPS, synchronous precursor selection.

(B) Comparison of selected gene ontology (GO) term enrichments of upregulated proteins (FC > 0.2, $p < 0.05$) in NPM1c (+doxycycline [Dox])- versus control (−Dox)-, NPM1wt (+Dox)- versus control (−Dox)-, and NPM1c (+Dox)- versus NPM1wt (+Dox)-expressing cells.

(C) Comparison of selected UniProt Keyword enrichments of downregulated proteins (FC ≤ -0.2, $p < 0.05$) of OCI-AML3 cells with endogenous NPM1c-FKBP12(F36V) upon 500 nM dTAG-13 treatment.

(D) Immunoblot of whole-cell fraction (WCF) and nuclear fraction (NF) of U-2 OS cell lysates with Tet-inducible Flag-NPM1 or Flag-NPM1c expression. Expression as in (A). Histone and tubulin are used as loading controls.

(E) Quantification of the lysosome count per cell by LysoTracker red staining in U-2 OS cells with Tet-inducible Flag-NPM1 or Flag-NPM1c expression as in (A). Cell lines were measured separately. Data are presented as mean ± SD, n = 5 biological replicates.

(F) Immunoblot of OCI-AML3 cell lysate after depletion of endogenous NPM1c by siRNA transfection after 72 h.

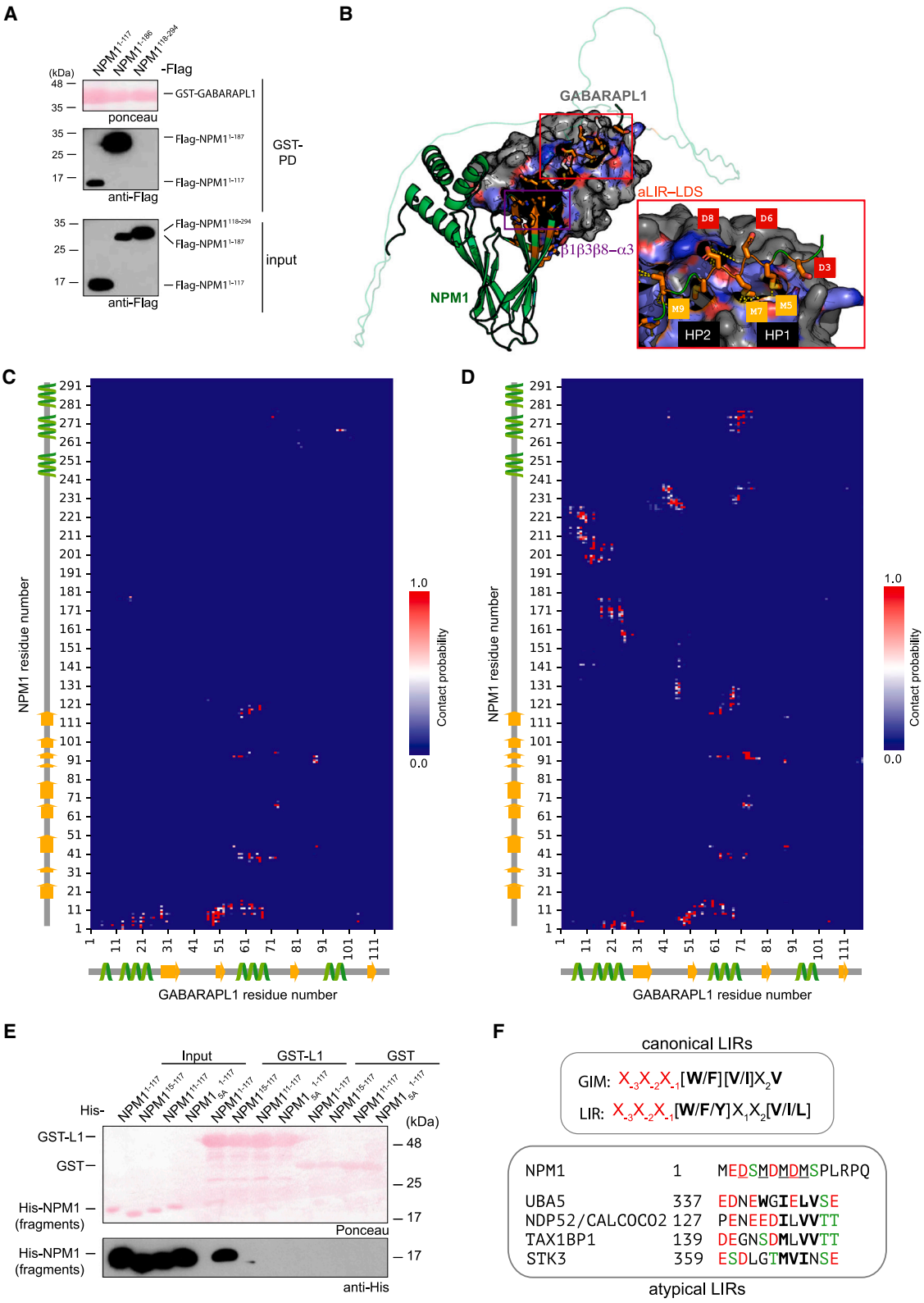

(legend on next page)

expression modulates TFEB phosphorylation status and its activation-associated translocation to the nucleus. By comparing TFEB levels in different cellular fractions, we observed a downshift of the TFEB band in whole-cell extracts upon NPM1 or NPM1c expression, indicative of its dephosphorylation. This is accompanied by a strong nuclear enrichment of TFEB that goes along with increased GABARAPL1 and LAMP1 levels, demonstrating that NPM1 impacts TFEB activation and nuclear localization (Figure 4D). In line, enhanced expression of NPM1 or NPM1c triggers a drastic increase in lysosome count as monitored by LysoTracker red staining (Figure 4E), most likely as a consequence of TFEB activation.

To further validate whether endogenous NPM1c regulates TFEB activity in AML cells, we depleted NPM1c from OCI-AML3 cells by siRNA and monitored phosphorylation of TFEB at S211 indicative of inactive TFEB (Figure 4F). Lack of NPM1c triggers an increase in phospho-TFEB (S211) levels correlating with a reduction of LAMP1 levels. Furthermore, removal of NPM1c from OCI-AML3 cells by targeted degradation is paralleled by phospho-TFEB induction in a process that can be blocked by mTOR inhibition (Figure S4E). As S211 is a known mTOR target site, we conclude that NPM1c-dependent regulation of TFEB depends on local mTOR activity. This fits our model that NPM1 and NPM1c interaction with GABARAPs locally modulates the activity of the V-ATPase-Ragulator complex. Altogether, these data indicate that NPM1 and NPM1c control autolysosome biogenesis through the activation of TFEB.

NPM1 and NPM1c bind to GABARAP family members through a non-canonical interaction motif

To determine whether the regulatory function of NPM1 in autolysosome induction directly depends on its ability to bind GABARAPs, we defined the interacting region within NPM1. As bioinformatic predictions using iLIR (https://ilir.warwick.ac.uk/search.php) did not reveal any characteristic canonical LIR motifs within the NPM1 or NPM1c sequences, we initially performed binding experiments to narrow down the region that binds to GABARAPL1. GST pull-down experiments using three distinct fragments of His-tagged NPM1 ($NPM1^{1-117}$, $NPM1^{1-186}$, or $NPM1^{118-294}$) and GST-GABARAPL1 demonstrated that the N-terminal core region ($NPM1^{1-117}$), comprising the N-terminal unstructured sequence (residues 1–14) and the oligomerization domain (15–117), is sufficient to bind to GST-GABARAPL1 (Figure 5A). Using a larger $NPM1^{1-186}$ fragment, additionally containing the intrinsically disordered central acidic region (IDR, 118–186), further strengthens the interaction to GST-GABARAPL1. However, without the N-terminal core part, the acidic region plus the C-terminal part ($NPM1^{118-294}$) does not mediate binding to GST-GABARAPL1. These data indicate that $NPM1^{1-117}$ is necessary and sufficient to bind to GABARAPL1. This also explains the interaction of GABARAPs with NPM1c, which differs from the wild-type protein only in its extreme C-terminal region.

To identify the exact binding site and the binding mode, we modeled the 3D structure of the NPM1-GABARAPL1 complex using AlphaFold2 (Figure 5B). The top 10 models show a consistent binding mode, where the N-terminal methionine-rich stretch ($NPM1_{1-15}$) mediated direct contacts and was anchored to the LDS of GABARAPL1 (Figures 5B, S5A, and S5B). Further, the β sheet (strands β1, β3, β8) residues also mediate interactions with the α3 helix of GABARAPL1, providing additional stability to the binary complex (Figures 5B and 5C). Atomistic molecular dynamics (MD) simulations of the NPM1-GABARAPL1 complex initiated from this structure revealed that the binding mode and the associated key interactions remained stable under the simulation timescale (Figures 5D and S5C, top). Furthermore, we found that the IDR of NPM1 mediated additional dynamic contacts with GABARAPL1. These interaction sites varied in the different models and displayed more dynamic contacts in the four replicates (Figures 5D and S5C, bottom). To test the significance of the N terminus of NPM1 in GABARAPL1 binding, we performed MD simulations with an N-terminal peptide $NPM1^{1-20}$ and a mutant peptide in complex with GABARAPL1. While $NPM1^{1-20}$ binds stably to GABARAPL1, $NPM1_{5A}{}^{1-20}$ displayed fewer contacts across the interface and disassociated swiftly under the MD timescale (Figure S5D; Videos S1 and S2).

To verify this binding model, we performed a peptide array-based screen to map potential GABARAPL1-interacting sites along NPM1 (Figure S5E). By screening 57 overlapping peptides (20-mers) covering $NPM1^{1-189}$ for binding with GABARAPL1, we found that the peptide spanning $NPM1^{1-20}$ showed strong signal intensities. Furthermore, GABARAPL1 also mediated weak interactions with peptides covering the central acidic domain of NPM1.

Motivated by these findings, we generated N-terminal deletion fragments and an alanine variant of NPM1 ($NPM1^{11-117}$,

Figure 5. NPM1 N terminus harbors an atypical LIR

(A) Immunoblot of a GST pull-down with immobilized GST-GABARAPL1 and HEK cell lysates expressing fragments of Flag-tagged NPM1.

(B) Top-ranked AlphaFold2 model of the NPM1-GABARAPL1 complex, highlighting the role of the N-terminal domain of NPM1 (green) interacting with GABARAPL1 (gray). Two interface regions are highlighted (boxes). Inset shows the zoom-up of the N-terminal methionine-rich aLIR segment (side chains shown as orange sticks and labeled) docked into the two hydrophobic pockets (HP1 and HP2) of the LDS with additional electrostatic interactions (positive/negative charge colored as blue/red). Yellow dashes indicate residue contacts within 4 Å.

(C) Contact map showing pairwise-residue interactions of NPM1 and GABARAPL1 averaged over the top 10 models. Interaction sites along NPM1 and GABARAPL1 are highlighted with schematics of the local secondary structure.

(D) Same as (C), but averaged over all 4 × 500 ns MD runs initiated from four different starting models. Non-specific and dynamic contacts emerge along the central IDR of NPM1 during these MD runs.

(E) Immunoblot of an *in vitro* interaction assay of immobilized GST-GABARAPL1 and His-NPM1 fragments purified from bacteria.

(F) Top: comparison of the consensus core sequence of the canonical GABARAP-interacting motifs (GIMs) and the LC3 interacting regions (LIRs). X, any residue; red X, negatively charged residue (D/E or phospho S/T). Bottom: alignment of GABARAPL1 interacting sites of NPM1 and previously identified atypical LIRs. Residues docking into the hydrophobic pockets of ATG8 proteins are shown in bold. Underlined residues of NPM1 aLIR are mutated to alanine ($NPM1_{5A}$). Negatively charged residues and potential phosphorylation sites are colored in red and green, respectively.

NPM1$^{15-117}$, and NPM1$_{5A}^{1-117}$). All three variants lose the ability to bind to GABARAPL1 (Figure 5E), validating our computational model and confirming that the very N-terminal region of NPM1 is essential for GABARAPL1 binding. Importantly, this region is methionine rich and lacks the characteristic aromatic amino acids of canonical LIR motifs. A detailed analysis of the interactions mediated by the N-terminal stretch in our top-ranked complex structures revealed four alternate configurations for methionines (M5, M7, and M9) directly docking into the LDS of GABARAPL1 (Figure S5B). Accordingly, we define this distinct GABARAP-binding motif of NPM1 as an aLIR (Figure 5F).

To dissect the residues of GABARAPL1 that bind to this aLIR, we performed GST pull-down assays of wild-type GST-GABARAPL1 or its variants with mutations in either the LDS or the UDS. We observed that alterations of critical residues in either the LDS (V51, F60) or the UDS (F77) affect binding to NPM1, suggesting that both regions could be involved in binding (Figure 6A). We next performed NMR-based interaction studies using ^{15}N-labeled GABARAPL1 and a 20-mer peptide covering the N-terminal stretch of NPM1 (NPM1$^{1-20}$) (Figures 6B and S6A). Chemical shift perturbation (CSP) measurements demonstrate that residues of HP1 (Y25 and L50) and HP2 (F60 and L63) of the LDS in GABARAPL1 are strongly involved in binding to NPM1$^{1-20}$ (Figures 6B, 6D, and S6A). In addition, K46 of GABARAPL1 also showed high CSP values, indicating the involvement of electrostatic interactions consistent with our models. Importantly, when using a corresponding peptide with five residues mutated to alanine (NPM1$_{5A}^{1-20}$), the above-mentioned CSP values are largely abrogated (Figures 6C and S6A).

To reaffirm the involvement of the LDS on NPM1 binding, we performed NMR measurements of GABARAPL1 with NPM1$^{1-117}$ and full-length NPM1^{fl} as well as their respective alanine mutants (NPM1$_{5A}$) (Figures S6B–S6E). The contact sites on GABARAPL1 interacting with NPM1$^{1-117}$ show an almost perfect overlap with the sites interacting with the NPM1$^{1-20}$ peptide, confirming the direct involvement of the LDS of GABARAPL1 in binding (Figures 6B, 6D, and S6B). Moreover, NMR data of GABARAPL1 with full-length NPM1 show high CSP values for the GABARAPL1 residues within the LDS (Figure S6D). However, the broadening of the corresponding peaks and the appearance of new peaks indicate the possible involvement of other GAPARAPL1 residues with full-length NPM1. In our biochemical data and MD simulations, we found that the interaction of full-length NPM1 with GABARAPL1 is additionally stabilized by dynamic interactions of the IDR (Figures 5A, 5D, and S5C), explaining the NMR observations. The effect of the 5A mutation on the full-length protein binding (NPM1$_{5a}^{fl}$) is less prominent in comparison with NPM1-derived peptide NPM1$^{1-20}$ and fragment NPM1$^{1-117}$ binding (Figures 6B, 6C, and S6B–S6E), presumably due to additional stabilizing interactions of the IDR.

By integrating data from binding assays, computational modeling, and NMR experiments, we propose that the methionine-rich N-terminal stretch of NPM1 interacts explicitly with the LDS in GABARAPL1 (Figure 6E). Furthermore, K46 of GABARAPL1 is likely engaged in an inter-molecular salt bridge with D8 of NPM1, further providing additional stability to the atypical LIR-LDS interaction (Figure 6E).

Interestingly, the aLIR of NPM1 contains two serine residues (S4 and S10), which can undergo phosphorylation.[36] By introducing phospho-mimicking mutants at these residues, we observed stronger binding of NPM1 to GABARAPL1 (Figure S6F). Notably, our computational models predict close proximity of S4 and S10 to basic residues (K24, 46, 48, R67, and K28) around the LDS, indicating that the negative charges of phosphoserines are likely engaged in electrostatic interactions, further stabilizing the aLIR-LDS interaction (Figure 6E).

Since acetylation of K46 and K48 of hATG8s interferes with LIR-LDS binding,[37] we tested the interaction of acetylation-mimicking mutants of GABARAPL1 (K46/48Q) with NPM1. Interestingly, GABARAPL1^{K46,48Q} did not bind to NPM1$^{1-117}$ and NPM1$^{1-189}$, further validating our interaction model (Figure S6G).

NPM1c-induced TFEB activation depends on the GABARAP binding module

To test whether binding of NPM1c to GABARAPs contributes to elevated autophagy of NPM1c-positive AML cells, we depleted the aLIR containing flexible N terminus of NPM1c. GST pull-down experiments confirmed that NPM1c$^{11-298}$ shows reduced binding to GST-GABARAPL1 compared with full-length NPM1c in a cellular context (Figure 7A). The remaining residual binding could either be due to oligomerization with endogenous NPM1 or result from a second binding site, as described above (Figure 5A). In line with the GST pull-down data, PLA assays reveal a reduced association of NPM1c$^{11-298}$ with GABARAPs compared with full-length NPM1c (Figure 7B). Importantly, this reduction is due to the loss of the N-terminal binding site and not due to changes in the subcellular distribution of NPM1c$^{11-298}$ when compared with full-length NPM1c (Figure 7C). In addition, we performed mass spectrometry analysis of co-immunoprecipitations of full-length NPM1c, NPM1c$^{11-298}$, and the respective wild-type proteins. We did not detect huge variation in the interactomes of NPM1 or NPM1c compared with their respective N-terminal truncation by performing a principal-component analysis (Figure S7A).

To explore whether the GABARAP binding N terminus affects the propensity of NPM1c or wild-type NPM1 to induce autophagic flux, we compared full-length NPM1c and NPM1c$^{11-298}$ and the respective wild-type proteins in the FACS-based autophagic flux assay described above (Figure 1A). Consistent with the data shown in Figure 1D, full-length NPM1 and NPM1c trigger a dose-dependent increase in autophagic flux (Figures 7D and S7B). By contrast, the GABARAP binding-deficient NPM1c$^{11-298}$ variant fails to induce autophagic flux, suggesting that the GABARAP-binding module of NPM1c is required for its pro-autophagic activity (Figure 7D). Notably, depletion of the N-terminal region of wild-type NPM1 does not reduce its autophagic propensity, arguing for a stronger dependency of NPM1c on the N-terminal region for autophagy induction (Figure S7B). We anticipate that the oligomerization with endogenous NPM1 or increased protein levels compared with NPM1c maintains the autophagic potential of NPM1$^{11-294}$.

To investigate whether the activation of TFEB by NPM1c depends on the N-terminal binding module, full-length NPM1c or NPM1c$^{11-298}$ were expressed in U-2 OS cells, and the nuclear distribution of TFEB was detected by immunoblotting. When

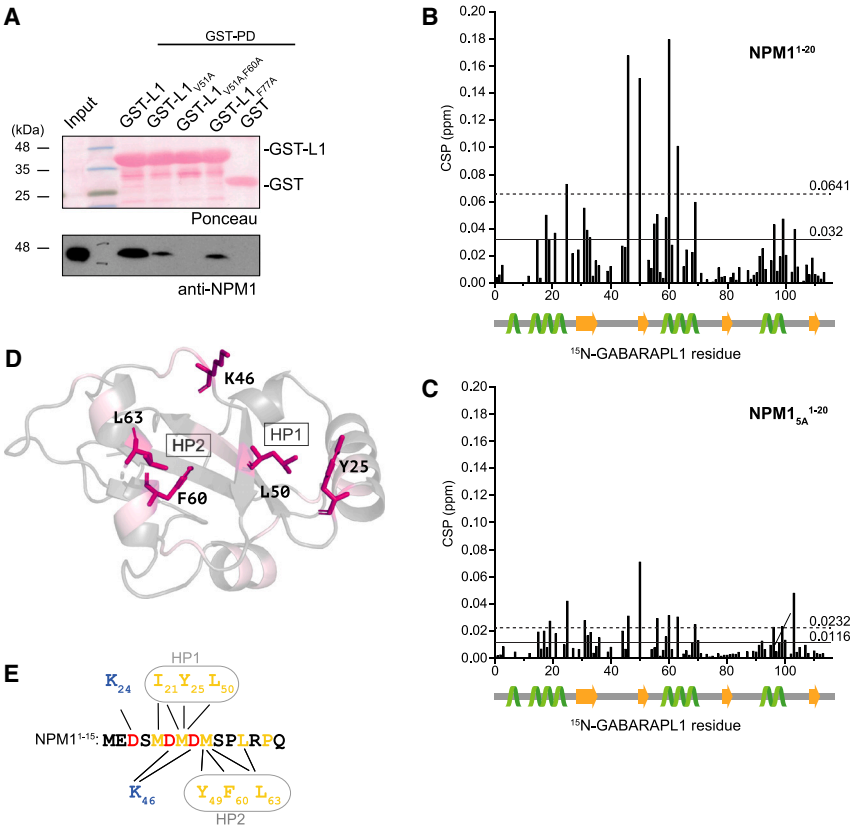

Figure 6. The atypical LIR of NPM1 binds to the LDS of GABARAPL1

(A) Immunoblot of a GST pull-down with immobilized GST, GST-GABARAPL1, and mutants of GST-GABARAPL1 and HEK cell lysate with an endogenous NPM1 antibody.

(B and C) Chemical shift perturbation (CSP) of ^{15}N-GABARAPL1 titrated with NPM1$^{1-20}$ (B) or NPM1$_{5A}^{1-20}$ (C) peptide in the ratio of 1:10 measured by NMR. Solid and dashed lines indicate 1× SD and 2× SD, respectively. A zero value indicates either no shift or that peaks could not be detected in the spectra. GABARAPL1 secondary structure is shown below.

(D) Mapping of residues with high CSP (B) onto the GABARAPL1 structure of the top-ranked AlphaFold2 model of NPM1-GABARAPL1 (Figure 5B). Residues with CSP values ≥ 2× SD and ≥ 1× SD are shown as sticks and highlighted in pink or light pink, respectively. The structure of NPM1 is not shown here. HP, hydrophobic pocket.

(E) Summary of the interaction between the N-terminal atypical LIR of NPM1 and the LDS of GABARAPL1 after mapping key residues from binding assays and NMR experiments and their contacts from modeling and simulations, respectively. Hydrophobic contacts (yellow residues) and electrostatic interactions (red/blue residues) across the LIR-LDS interface are shown.

compared with full-length NPM1c, expression of NPM1c$^{11-298}$ results in reduced levels of nuclear TFEB and less pronounced *GABARAPL1* mRNA induction (Figures 7E and 7F).

Previous work has proposed that NPM1c stimulates autophagy by stabilizing the ULK1 kinase.[38] Therefore, we compared ULK1 protein levels in cells expressing either full-length NPM1c or NPM1c$^{11-298}$ under control conditions and starvation (Figure S7C). In line with previous work, expression of NPM1c leads to an increase in ULK1 correlating with enhanced phosphorylation of the ULK1 substrate ATG14. By contrast, the GABARAP-binding-deficient NPM1c$^{11-298}$ variant exhibits a reduced potential in stabilizing ULK1; accordingly, its substrate ATG14 phosphorylation is less pronounced. These data indicate that the N terminus of NPM1c is also critical for ULK1-dependent early steps of autophagy induction. Altogether, these data demonstrate that the N-terminal GABARAP binding module of NPM1c is critical for the pro-autophagic potential of NPM1c and the activation of TFEB.

DISCUSSION

Members of the hATG8 family orchestrate autophagy, a highly regulated process. However, it is still unclear how distinct hATG8 subfamilies, e.g., members of the LC3 and the GABARAP branch, regulate the autophagy-lysosome network. Here, we show that the nucleolar scaffold protein NPM1 and its predominantly cytosolic AML-associated variant NMP1c stimulate the autophagic flux and specifically bind to the GABARAP subfamily of hATG8 proteins. Our data indicate that the imbalance of autophagy observed in NPM1c-positive AML is directly linked to the control of autolysosome biogenesis.

We reveal an unprecedented interaction mode of NPM1 and NPM1c with GABARAPL1. Our combined computational modeling and NMR studies uncover an atypical interaction of the N-terminal region of NPM1 with the LDS of GABARAPL1.[16] The aLIR we identified here lacks the characteristic aromatic residue that is a hallmark of both canonical LIRs as well as selective GABARAP interaction motifs (Figure 5F).[39] Binding of the aLIR of NPM1 and NPM1c to GABARAPs relies on a so-far unknown interaction mode that is based on the presence of methionine residues. While the clustering of methionine is a particular feature of NPM1's aLIR, the clustering of acidic or phosphorylated residues is common with canonical LIRs. Conceptionally, we demonstrate that AlphaFold2-based modeling provides a powerful tool to identify not only canonical ATG8 interactions[40] but also more distantly related sequence motifs.

NPM1 also exhibits structural polymorphism. Importantly, its N-terminal domain harbors an acidic loop that exhibits a high degree of flexibility, allowing a switch from a folded pentamer to a disordered monomeric state.[41] Furthermore, progressive multisite phosphorylation of NPM1 within its N-terminal domain modulates its oligomerization state, pushing this equilibrium toward monomers.

The potential involvement of PTMs, e.g., phosphorylation of NPM1 at S4 and S10 within the aLIR of NPM1, indicates that the interaction can be regulated depending on distinct signaling events. Notably, S4 and S10 in NPM1 are targeted by the mitotic kinase PLK1, suggesting a cell-cycle-dependent control of GABARAP-NPM1 interaction.[36] Intriguingly,

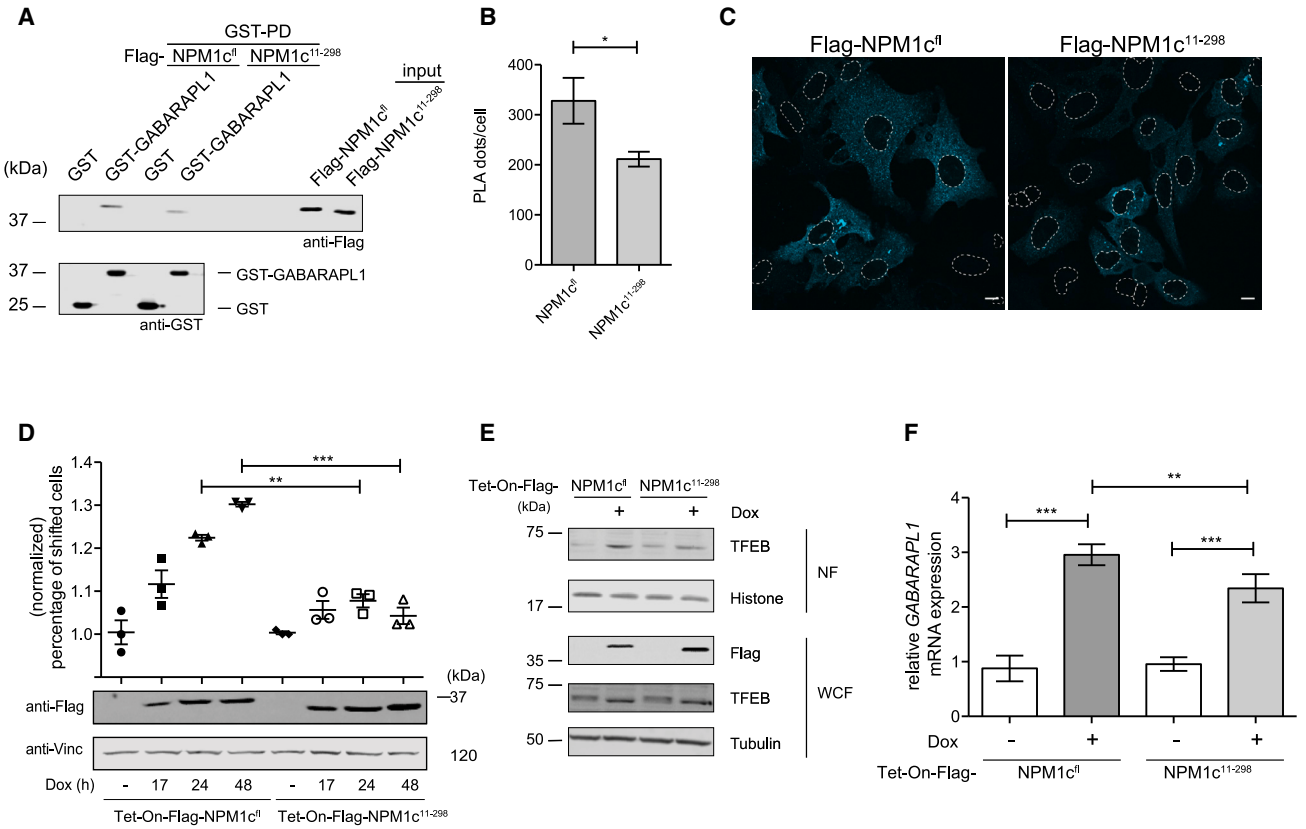

Figure 7. Pro-autophagic property of NPM1c is GABARAP-binding dependent

(A) Immunoblot of a GST pull-down with immobilized GST-GABARAPL1 and HEK lysate with Flag-NPM1c and Flag-NPM1c$^{11-298}$ expression.

(B) Quantification of a PLA using Flag and endogenous GABARAP antibodies in U-2 OS cells expressing Flag-NPM1c or Flag-NPM1c$^{11-298}$ under a Tet-inducible promotor. Cells are additionally depleted of endogenous NPM1 with siRNA. Data are presented as mean ± SEM. At least 32 cells are counted per condition. *$p < 0.05$, as analyzed by a two-sided t test.

(C) Fluorescence images of U-2 OS cells expressing Flag-NPM1c or Flag-NPM1c$^{11-298}$ under a Tet-inducible promotor from (B) using a Flag-specific antibody. Scale bar, 10 μm.

(D) Quantification of flow cytometric analysis of U-2 OS$^{GFP-LC3B-RFP-LC3B\Delta G}$ with Tet-inducible Flag-NPM1c or Flag-NPM1c$^{11-298}$, treated with doxycycline (0.1 μg/mL) for the indicated time points. Data are presented as mean ± SD of the normalized percentage of cells in the autophagy-positive gate, n = 3 biological replicates, **$p < 0.01$, ***$p < 0.001$. Immunoblots (below) serve to control expression levels.

(E) Immunoblots with whole-cell fraction (WCF) and nuclear fraction (NF) of U-2 OS cell lysates with Tet-inducible Flag- NPM1c or Flag-NPM1c$^{11-298}$ expression for 24 h with 0.1 μg/mL doxycycline. Histone and tubulin are used as loading controls. Blots from Flag-NPM1c^{fl}-expressing cells are the same as in Figure 4D.

(F) qPCR analysis of GABARAPL1 mRNA normalized to *GAPDH* mRNA levels of U-2 OS cells with Tet-inducible Flag-NPM1c or Flag-NPM1c$^{11-298}$ expression as in (E). Data are presented as mean ± SD, n = 4 biological replicates, **$p < 0.01$, ***$p < 0.001$, as analyzed by one-way ANOVA followed by Tukey's multiple comparison test.

the binding of NPM1 is specific for the GABARAP subfamily of the hATG8 proteins. The exact molecular determinants for this specificity are currently unknown. Notably, however, most members of the autophagy core machinery display specificity for the GABARAP family proteins.[42] Importantly, it has been proposed that acidic residues at the C-terminal to a core LIR sequence, which are also present in NPM1, determine the selectivity for GABARAP proteins.[43] Furthermore, residues important for GABARAP-specific subfamily interaction in the LDS, such as Y25, F60, and L63, contribute to the aLIR-NPM1 binding.[44]

Our functional data reveal a crucial role for NPM1 in the regulation of autophagy. Depletion of NPM1 in U-2 OS cells affects autophagosome formation, lysosome biogenesis, and autophagic flux, demonstrating the requirement of NPM1 in promoting or maintaining the capacity of the autolysosomal system. In accordance with this idea, enhanced expression of NPM1 drives the autophagic flux and promotes autolysosome biogenesis. Importantly, the AML-associated NPM1c also shows pro-autophagic activity, which depends on the aLIR-containing N-terminal domain. It is currently unclear why deletion of the N-terminal region from wild-type NPM1 (NPM1$^{11-294}$) does not affect its autophagic propensity. We anticipate that the higher expression levels of NPM1$^{11-294}$ or its oligomerization with endogenous NPM1 compensate for the lack of the N terminus. Noteworthy, in contrast to siRNA-mediated depletion of NPM1c from the NPM1c-positive OCI-AML3 cell line, downregulation of wild-type NPM1

from NPM1c-negative Hel276 and MV4-11 does not affect the autophagic flux, supporting our conclusion that NPM1c has a specific impact on autophagy in AML.

NPM1 is a multifunctional protein involved in various cellular activities and assists in the nucleo-cytoplasmic transport of proteins.[45–47] Since autophagy induction involves the transfer of hATG8 proteins from the nucleus to the cytosol, NPM1 and NPM1c could exhibit their pro-autophagic potential by aiding the transfer of GABARAP proteins to the cytosol or by stabilizing it in the cytosol.[37] NPM1 may have a distinct role in the spatial control of GABARAP proteins at centrosomes.[10,48–50] Notably, wild-type NPM1 shuttles between the nucleus and the cytosol, likely explaining its impact on the largely cytosolic events of autophagic processes. We propose that NPM1c fosters these processes due to its constitutive cytosolic localization.

GABARAP family proteins control both the early and late steps of autophagy. At the initiation stage, the binding of GABARAPs to ULK1 and ATG13 is essential for activating ULK1 and the subsequent autophagosome formation.[10,42] Here, we confirm previous work demonstrating that expression of the NPM1c variant leads to increased ULK1 levels correlating with enhanced phosphorylation of its substrate ATG14.[51] These effects largely depend on the presence of the aLIR containing the N-terminal stretch of NPM1c. Therefore, we propose that NPM1c directly exerts its effects on ULK1 by increasing GABARAPL1 protein levels rather than indirectly through TRAF6 inactivation. Furthermore, TFEB-mediated transcriptional upregulation of ULK1 by NPM1c likely contributes to the observed increase in ULK1 levels. Despite these observations, we observed only moderate activation of ULK1 by NPM1c, indicating that its pro-autophagic propensity is not solely dependent on this process.

In addition to their role in autophagy initiation, GABARAPs exert distinct regulatory functions at later stages in the autophagy-lysosome pathway, in particular during autolysosome fusion and V-ATPase-dependent lysosome biogenesis.[11,33,52,53] GABARAPs, but not LC3 proteins, are essential to stimulate autophagy and lysosomal gene expression via activation of TFEB, the master transcription regulator of the autophagy-lysosomal pathway.[54,55] Under nutrient-rich conditions, TFEB is kept inactive through phosphorylation by mTOR. This is mediated by the V-ATPase-Ragulator complex, which triggers local activation of mTOR at the lysosomal membrane. During starvation, the V-ATPase-Ragulator complex senses the lack of amino acids in the lysosomal lumen, leading to mTOR release and causing TFEB dephosphorylation, activation, and nuclear translocation. Although the molecular details are not fully understood, it is well established that GABARAP family members are necessary for the V-ATPase-dependent TFEB activation.[9,33] GABARAP-mediated TFEB activation can be modulated by factors such as NUFIP2 or the FLCN/FNIP1/2 complex, which depends on their interaction with GABARAPs.[9] We propose that NPM1 and NPM1c significantly impact the autolysosome system by primarily controlling the activation of TFEB. Our proteomic data suggest that NPM1 controls the association of GABARAPL1 with components of the V-ATPase. However, it is currently unclear whether the association of the V-ATPase with GABARAPL1 occurs through lipidated or unlipidated GABARAPL1. Furthermore, we demonstrate that elevated expression of NPM1 and NPM1c stimulate the nuclear translocation of TFEB in a process that largely depends on the binding of NPM1 to GABARAP proteins.

Consequently, the expression of NPM1 or NPM1c leads to the upregulation of lysosomal and autophagosomal proteins controlled by TFEB. As we did not observe NPM1 or NPM1c interaction with GABARAP proteins on autophagosomes or autolysosomes, we anticipate that NPM1/NPM1c acts more indirectly by controlling the availability of GABARAPs to function on autophagosomes and autolysosomes. Since TFEB controls the expression of GABARAP proteins themselves, elevated NPM1 and NPM1c drive a feedforward loop to amplify the autophagic process. This idea aligns with the strong increase of *GABARAPL1* mRNA and GABARAPL1 protein levels detected upon expression of NPM1 or NPM1c.

High NPM1 expression in solid tumors is typically associated with a poor prognosis. So far, this has been correlated with NPM1's role in ribosome biogenesis, but our data suggest that it may also be linked to the activation of autophagy. Expression of NPM1c is widely accepted as an oncogenic driver for AML formation. In NPM1c-positive AML, autophagy is activated leading to leukemic cell survival.[38] Although this has been linked to the activation of several pro-autophagic signaling pathways,[51,56,57] our data provide a unifying and overarching model of NPM1c-induced autophagy that relies on the GABARAP binding module and the activation of TFEB. We demonstrate that targeted degradation of NPM1c in OCI-AML3 cells triggers a downregulation of autophagosome/lysosome regulators, accompanied by the induction of the inhibitory TFEB phosphorylation. We propose that, through its constitutive delocalization to the cytosol, NPM1c greatly exacerbates the physiological role of NPM1 in the autophagy-lysosome pathway. Targeting the interaction of GABARAPs and NPM1c may thus open a future therapeutic avenue in treating NPM1c-positive AML.

Limitations of the study

We demonstrate that NPM1wt and NPM1c interact with GABARAP proteins via non-canonical aLIR-LDS interaction. While this interaction is important for the pro-autophagic potential of NPM1c, we could not show this for NPM1. In line with this observation, we showed that the autophagic flux in NPM1c-positive AML cells depends on NPM1c, but in NPM1c-negative AML cells this seems to be independent of NPM1. At this stage, we cannot fully explain the mechanistic basis of the cell- and context-specific differences in the pro-autophagic potential of NPM1 and NPM1c. To conclusively address this point, a larger panel of cell lines and *in vivo* mouse models are needed. Furthermore, it remains to be determined how binding of GABARAPs to NPM1 and NPM1c mediates V-ATPase-regulated TFEB activity. Moreover, future work needs to address how this pathway can be exploited in NPM1c-positive AML comprising additional genetic alterations.[23]

STAR★METHODS

Detailed methods are provided in the online version of this paper and include the following:

SUPPLEMENTAL INFORMATION

Supplemental information can be found online at https://doi.org/10.1016/j.celrep.2023.113484.

ACKNOWLEDGMENTS

This work was funded by the Deutsche Forschungsgemeinschaft (DFG) SFB/CRC1177, grant/award no. Project-ID 259130777-SFB1177 (to C.L., R.M.B., H.M., S.M., A.C., I.D., G.T., C.M., A.K., V.D., A.B., and C.H.B.). S.M. is supported by DFG grant MU-1764/6, Project-ID 465470262 and DFG grant MU-1764/7, Project-ID 494535244. This research used the Goethe-HLR cluster and computational resources from the Center for Scientific Computing, Goethe University Frankfurt. S.A.P.C., R.M.B., and S.M. are supported by the Clusterproject ENABLE funded by the Hessian Ministry for Science and the Arts. V.V.R. is supported by the Structural Genomics Consortium (SGC). We thank the Quantitative Proteomics Unit at IBC2 (Goethe University, Frankfurt), particularly Martin Adrian-Allgood, for technical assistance, Kristina Wagner for producing nano-LC columns, and David Krause for help in (bio)informatics. We thank Marc Sawatzki for generating initial preliminary data in this project. We thank the DFG for funding of the LC-MS systems, namely the easy nLC 1200, QExactive HF (Project-ID 259130777, SFB1177—Selective Autophagy), and the easy nLC1200, Orbitrap Fusion LUMOS (FuGG Project-ID 403765277), as well as the European Fonds for regional development (REACT-EU, IWB-EFRE-program Hessen, 20008763) for the VanquishNeo, Orbitrap Ascend LC-MS systems.

AUTHOR CONTRIBUTIONS

S.M. supervised the project. H.M. performed the biochemical and cell biological experiments. C.L. and S.A.P.C. performed structural modeling, MD simulations, and analysis of all simulation data with support from R.M.B. A.K. performed the NMR experiments with the help of F.L. under supervision of V.D. and V.V.R. A.C.-P. provided support for microscopic analysis and conceptualization of the project. G.T. ran the mass spectrometers and supported H.M. in data analysis. S.E.K., I.D., C.M., A.B., L.B., C.H.B., and H.U. provided reagents, cell lines, and critical scientific input. H.M., R.M.B., and S.M. wrote the initial draft. All authors reviewed the manuscript giving valuable comments.

DECLARATION OF INTERESTS

The authors declare no competing interests.

Received: March 29, 2023
Revised: September 22, 2023
Accepted: November 8, 2023
Published: November 22, 2023

REFERENCES

1. Lamark, T., and Johansen, T. (2021). Mechanisms of Selective Autophagy. Annu. Rev. Cell Dev. Biol. *37*, 143–169.
2. Yu, L., Chen, Y., and Tooze, S.A. (2018). Autophagy pathway: Cellular and molecular mechanisms. Autophagy *14*, 207–215.
3. Kang, C., and Avery, L. (2008). To be or not to be, the level of autophagy is the question: dual roles of autophagy in the survival response to starvation. Autophagy *4*, 82–84.
4. Hosokawa, N., Hara, T., Kaizuka, T., Kishi, C., Takamura, A., Miura, Y., Iemura, S.i., Natsume, T., Takehana, K., Yamada, N., et al. (2009). Nutrient-dependent mTORC1 association with the ULK1-Atg13-FIP200 complex required for autophagy. Mol. Biol. Cell *20*, 1981–1991.
5. Jung, C.H., Jun, C.B., Ro, S.H., Kim, Y.M., Otto, N.M., Cao, J., Kundu, M., and Kim, D.H. (2009). ULK-Atg13-FIP200 complexes mediate mTOR signaling to the autophagy machinery. Mol. Biol. Cell *20*, 1992–2003.
6. Rogov, V., Dötsch, V., Johansen, T., and Kirkin, V. (2014). Interactions between autophagy receptors and ubiquitin-like proteins form the molecular basis for selective autophagy. Mol. Cell *53*, 167–178.
7. Wesch, N., Kirkin, V., and Rogov, V.V. (2020). Atg8-Family Proteins-Structural Features and Molecular Interactions in Autophagy and Beyond. Cells *9*.
8. Weidberg, H., Shvets, E., Shpilka, T., Shimron, F., Shinder, V., and Elazar, Z. (2010). LC3 and GATE-16/GABARAP subfamilies are both essential yet act differently in autophagosome biogenesis. EMBO J. *29*, 1792–1802.
9. Goodwin, J.M., Walkup, W.G., 4th, Hooper, K., Li, T., Kishi-Itakura, C., Ng, A., Lehmberg, T., Jha, A., Kommineni, S., Fletcher, K., et al. (2021). GABARAP sequesters the FLCN-FNIP tumor suppressor complex to couple autophagy with lysosomal biogenesis. Sci. Adv. *7*, eabj2485.
10. Joachim, J., and Tooze, S.A. (2016). GABARAP activates ULK1 and traffics from the centrosome dependent on Golgi partners WAC and GOLGA2/GM130. Autophagy *12*, 892–893.
11. Johansen, T., and Lamark, T. (2020). Selective Autophagy: ATG8 Family Proteins, LIR Motifs and Cargo Receptors. J. Mol. Biol. *432*, 80–103.
12. Birgisdottir, Å.B., Lamark, T., and Johansen, T. (2013). The LIR motif - crucial for selective autophagy. J. Cell Sci. *126*, 3237–3247.
13. Noda, N.N., Ohsumi, Y., and Inagaki, F. (2010). Atg8-family interacting motif crucial for selective autophagy. FEBS Lett. *584*, 1379–1385.
14. Rogov, V.V., Suzuki, H., Fiskin, E., Wild, P., Kniss, A., Rozenknop, A., Kato, R., Kawasaki, M., McEwan, D.G., Löhr, F., et al. (2013). Structural basis for phosphorylation-triggered autophagic clearance of Salmonella. Biochem. J. *454*, 459–466.
15. Wild, P., Farhan, H., McEwan, D.G., Wagner, S., Rogov, V.V., Brady, N.R., Richter, B., Korac, J., Waidmann, O., Choudhary, C., et al. (2011). Phosphorylation of the autophagy receptor optineurin restricts Salmonella growth. Science *333*, 228–233.
16. Huber, J., Obata, M., Gruber, J., Akutsu, M., Löhr, F., Rogova, N., Güntert, P., Dikic, I., Kirkin, V., Komatsu, M., et al. (2020). An atypical LIR motif

within UBA5 (ubiquitin like modifier activating enzyme 5) interacts with GABARAP proteins and mediates membrane localization of UBA5. Autophagy *16*, 256–270.

17. von Muhlinen, N., Akutsu, M., Ravenhill, B.J., Foeglein, Á., Bloor, S., Rutherford, T.J., Freund, S.M.V., Komander, D., and Randow, F. (2012). LC3C, bound selectively by a noncanonical LIR motif in NDP52, is required for antibacterial autophagy. Mol. Cell *48*, 329–342.
18. Aman, Y., Schmauck-Medina, T., Hansen, M., Morimoto, R.I., Simon, A.K., Bjedov, I., Palikaras, K., Simonsen, A., Johansen, T., Tavernarakis, N., et al. (2021). Autophagy in healthy aging and disease. Nat. Aging *1*, 634–650.
19. Klionsky, D.J., Petroni, G., Amaravadi, R.K., Baehrecke, E.H., Ballabio, A., Boya, P., Bravo-San Pedro, J.M., Cadwell, K., Cecconi, F., Choi, A.M.K., et al. (2021). Autophagy in major human diseases. EMBO J. *40*, e108863.
20. Koschade, S.E., and Brandts, C.H. (2020). Selective Autophagy in Normal and Malignant Hematopoiesis. J. Mol. Biol. *432*, 261–282.
21. Koschade, S.E., Klann, K., Shaid, S., Vick, B., Stratmann, J.A., Thölken, M., Meyer, L.M., Nguyen, T.D., Campe, J., Moser, L.M., et al. (2022). Translatome proteomics identifies autophagy as a resistance mechanism to on-target FLT3 inhibitors in acute myeloid leukemia. Leukemia *36*, 2396–2407.
22. Qiu, S., Kumar, H., Yan, C., Li, H., Paterson, A.J., Anderson, N.R., He, J., Yang, J., Xie, M., Crossman, D.K., et al. (2022). Autophagy inhibition impairs leukemia stem cell function in FLT3-ITD AML but has antagonistic interactions with tyrosine kinase inhibition. Leukemia *36*, 2621–2633.
23. Ranieri, R., Pianigiani, G., Sciabolacci, S., Perriello, V.M., Marra, A., Cardinali, V., Pierangeli, S., Milano, F., Gionfriddo, I., Brunetti, L., et al. (2022). Current status and future perspectives in targeted therapy of NPM1-mutated AML. Leukemia *36*, 2351–2367.
24. Shi, Y., Xue, Y., Wang, C., and Yu, L. (2022). Nucleophosmin 1: from its pathogenic role to a tantalizing therapeutic target in acute myeloid leukemia. Hematology *27*, 609–619.
25. Grisendi, S., Mecucci, C., Falini, B., and Pandolfi, P.P. (2006). Nucleophosmin and cancer. Nat. Rev. Cancer *6*, 493–505.
26. Falini, B., Brunetti, L., Sportoletti, P., and Martelli, M.P. (2020). NPM1-mutated acute myeloid leukemia: from bench to bedside. Blood *136*, 1707–1721.
27. Falini, B., Mecucci, C., Tiacci, E., Alcalay, M., Rosati, R., Pasqualucci, L., La Starza, R., Diverio, D., Colombo, E., Santucci, A., et al. (2005). Cytoplasmic nucleophosmin in acute myelogenous leukemia with a normal karyotype. N. Engl. J. Med. *352*, 254–266.
28. Kaizuka, T., Morishita, H., Hama, Y., Tsukamoto, S., Matsui, T., Toyota, Y., Kodama, A., Ishihara, T., Mizushima, T., and Mizushima, N. (2016). An Autophagic Flux Probe that Releases an Internal Control. Mol. Cell *64*, 835–849.
29. Du, W., Li, J., Sipple, J., Chen, J., and Pang, Q. (2010). Cytoplasmic FANCA-FANCC complex interacts and stabilizes the cytoplasm-dislocalized leukemic nucleophosmin protein (NPMc). J. Biol. Chem. *285*, 37436–37444.
30. Kimura, S., Noda, T., and Yoshimori, T. (2007). Dissection of the autophagosome maturation process by a novel reporter protein, tandem fluorescent-tagged LC3. Autophagy *3*, 452–460.
31. Wild, P., McEwan, D.G., and Dikic, I. (2014). The LC3 interactome at a glance. J. Cell Sci. *127*, 3–9.
32. Jewell, J.L., Russell, R.C., and Guan, K.L. (2013). Amino acid signalling upstream of mTOR. Nat. Rev. Mol. Cell Biol. *14*, 133–139.
33. Kumar, S., Jain, A., Choi, S.W., da Silva, G.P.D., Allers, L., Mudd, M.H., Peters, R.S., Anonsen, J.H., Rusten, T.E., Lazarou, M., and Deretic, V. (2020). Mammalian Atg8 proteins and the autophagy factor IRGM control mTOR and TFEB at a regulatory node critical for responses to pathogens. Nat. Cell Biol. *22*, 973–985.
34. Brunetti, L., Gundry, M.C., Sorcini, D., Guzman, A.G., Huang, Y.H., Ramabadran, R., Gionfriddo, I., Mezzasoma, F., Milano, F., Nabet, B., et al. (2018). Mutant NPM1 Maintains the Leukemic State through HOX Expression. Cancer Cell *34*, 499–512.e9.
35. Wang, X.Q.D., Fan, D., Han, Q., Liu, Y., Miao, H., Wang, X., Li, Q., Chen, D., Gore, H., Himadewi, P., et al. (2023). Mutant NPM1 Hijacks Transcriptional Hubs to Maintain Pathogenic Gene Programs in Acute Myeloid Leukemia. Cancer Discov. *13*, 724–745.
36. Zhang, H., Shi, X., Paddon, H., Hampong, M., Dai, W., and Pelech, S. (2004). B23/nucleophosmin serine 4 phosphorylation mediates mitotic functions of polo-like kinase 1. J. Biol. Chem. *279*, 35726–35734.
37. Huang, R., Xu, Y., Wan, W., Shou, X., Qian, J., You, Z., Liu, B., Chang, C., Zhou, T., Lippincott-Schwartz, J., and Liu, W. (2015). Deacetylation of nuclear LC3 drives autophagy initiation under starvation. Mol. Cell *57*, 456–466.
38. Du, W., Xu, A., Huang, Y., Cao, J., Zhu, H., Yang, B., Shao, X., He, Q., and Ying, M. (2021). The role of autophagy in targeted therapy for acute myeloid leukemia. Autophagy *17*, 2665–2679.
39. Rogov, V.V., Stolz, A., Ravichandran, A.C., Rios-Szwed, D.O., Suzuki, H., Kniss, A., Löhr, F., Wakatsuki, S., Dötsch, V., Dikic, I., et al. (2017). Structural and functional analysis of the GABARAP interaction motif (GIM). EMBO Rep. *18*, 1382–1396.
40. Cristiani, A., Dutta, A., Poveda-Cuevas, S.A., Kern, A., and Bhaskara, R.M. (2023). Identification of potential selective autophagy receptors from protein-content profiling of autophagosomes. J. Cell. Biochem.
41. Mitrea, D.M., Grace, C.R., Buljan, M., Yun, M.K., Pytel, N.J., Satumba, J., Nourse, A., Park, C.G., Madan Babu, M., White, S.W., and Kriwacki, R.W. (2014). Structural polymorphism in the N-terminal oligomerization domain of NPM1. Proc. Natl. Acad. Sci. USA *111*, 4466–4471.
42. Alemu, E.A., Lamark, T., Torgersen, K.M., Birgisdottir, A.B., Larsen, K.B., Jain, A., Olsvik, H., Øvervatn, A., Kirkin, V., and Johansen, T. (2012). ATG8 family proteins act as scaffolds for assembly of the ULK complex: sequence requirements for LC3-interacting region (LIR) motifs. J. Biol. Chem. *287*, 39275–39290.
43. Birgisdottir, Å.B., Mouilleron, S., Bhujabal, Z., Wirth, M., Sjøttem, E., Evjen, G., Zhang, W., Lee, R., O'Reilly, N., Tooze, S.A., et al. (2019). Members of the autophagy class III phosphatidylinositol 3-kinase complex I interact with GABARAP and GABARAPL1 via LIR motifs. Autophagy *15*, 1333–1355.
44. Sora, V., Kumar, M., Maiani, E., Lambrughi, M., Tiberti, M., and Papaleo, E. (2020). Structure and Dynamics in the ATG8 Family From Experimental to Computational Techniques. Front. Cell Dev. Biol. *8*, 420.
45. Colombo, E., Alcalay, M., and Pelicci, P.G. (2011). Nucleophosmin and its complex network: a possible therapeutic target in hematological diseases. Oncogene *30*, 2595–2609.
46. López, D.J., Rodríguez, J.A., and Bañuelos, S. (2020). Nucleophosmin, a multifunctional nucleolar organizer with a role in DNA repair. Biochim. Biophys. Acta. Proteins Proteom. *1868*, 140532.
47. Yu, Y., Maggi, L.B., Jr., Brady, S.N., Apicelli, A.J., Dai, M.S., Lu, H., and Weber, J.D. (2006). Nucleophosmin is essential for ribosomal protein L5 nuclear export. Mol. Cell Biol. *26*, 3798–3809.
48. Joachim, J., and Tooze, S.A. (2017). Centrosome to autophagosome signaling: Specific GABARAP regulation by centriolar satellites. Autophagy *13*, 2113–2114.
49. Reboutier, D., Troadec, M.B., Cremet, J.Y., Fukasawa, K., and Prigent, C. (2012). Nucleophosmin/B23 activates Aurora A at the centrosome through phosphorylation of serine 89. J. Cell Biol. *197*, 19–26.
50. Shinmura, K., Tarapore, P., Tokuyama, Y., George, K.R., and Fukasawa, K. (2005). Characterization of centrosomal association of nucleophosmin/B23 linked to Crm1 activity. FEBS Lett. *579*, 6621–6634.
51. Tang, Y., Tao, Y., Wang, L., Yang, L., Jing, Y., Jiang, X., Lei, L., Yang, Z., Wang, X., Peng, M., et al. (2021). NPM1 mutant maintains ULK1 protein stability via TRAF6-dependent ubiquitination to promote autophagic cell survival in leukemia. FASEB J *35*, e21192.
52. Kumar, S., Jain, A., Choi, S.W., Peixoto Duarte da Silva, G., Allers, L., Mudd, M.H., Peters, R.S., Anonsen, J.H., Rusten, T.E., Lazarou, M., and Deretic, V. (2020). Mammalian Atg8-family proteins are upstream

regulators of the lysosomalsystem by controlling MTOR and TFEB. Autophagy *16*, 2305–2306.

53. Nakamura, S., Akayama, S., and Yoshimori, T. (2022). Non-canonical roles of ATG8 for TFEB activation. Biochem. Soc. Trans. *50*, 47–54.
54. Sardiello, M., Palmieri, M., di Ronza, A., Medina, D.L., Valenza, M., Gennarino, V.A., Di Malta, C., Donaudy, F., Embrione, V., Polishchuk, R.S., et al. (2009). A gene network regulating lysosomal biogenesis and function. Science *325*, 473–477.
55. Settembre, C., Di Malta, C., Polito, V.A., Garcia Arencibia, M., Vetrini, F., Erdin, S., Erdin, S.U., Huynh, T., Medina, D., Colella, P., et al. (2011). TFEB links autophagy to lysosomal biogenesis. Science *332*, 1429–1433.
56. Wang, L., Yang, L., Yang, Z., Tang, Y., Tao, Y., Zhan, Q., Lei, L., Jing, Y., Jiang, X., Jin, H., et al. (2019). Glycolytic Enzyme PKM2 Mediates Autophagic Activation to Promote Cell Survival in NPM1-Mutated Leukemia. Int. J. Biol. Sci. *15*, 882–894.
57. Zou, Q., Tan, S., Yang, Z., Zhan, Q., Jin, H., Xian, J., Zhang, S., Yang, L., Wang, L., and Zhang, L. (2017). NPM1 Mutant Mediated PML Delocalization and Stabilization Enhances Autophagy and Cell Survival in Leukemic Cells. Theranostics *7*, 2289–2304.
58. Hertel, A., Alves, L.M., Dutz, H., Tascher, G., Bonn, F., Kaulich, M., Dikic, I., Eimer, S., Steinberg, F., and Bremm, A. (2022). USP32-regulated LAMTOR1 ubiquitination impacts mTORC1 activation and autophagy induction. Cell Rep. *41*, 111653.
59. Haindl, M., Harasim, T., Eick, D., and Muller, S. (2008). The nucleolar SUMO-specific protease SENP3 reverses SUMO modification of nucleophosmin and is required for rRNA processing. EMBO Rep. *9*, 273–279.
60. Kirkin, V., Lamark, T., Sou, Y.S., Bjørkøy, G., Nunn, J.L., Bruun, J.A., Shvets, E., McEwan, D.G., Clausen, T.H., Wild, P., et al. (2009). A role for NBR1 in autophagosomal degradation of ubiquitinated substrates. Mol. Cell *33*, 505–516.
61. Bornkamm, G.W., Berens, C., Kuklik-Roos, C., Bechet, J.M., Laux, G., Bachl, J., Korndoerfer, M., Schlee, M., Hölzel, M., Malamoussi, A., et al. (2005). Stringent doxycycline-dependent control of gene activities using an episomal one-vector system. Nucleic Acids Res. *33*, e137.
62. Jumper, J., Evans, R., Pritzel, A., Green, T., Figurnov, M., Ronneberger, O., Tunyasuvunakool, K., Bates, R., Žídek, A., Potapenko, A., et al. (2021). Highly accurate protein structure prediction with AlphaFold. Nature *596*, 583–589.
63. Evans, R., O'Neill, M., Pritzel, A., Antropova, N., Senior, A., Green, T., Žídek, A., Bates, R., Blackwell, S., Yim, J., et al. (2022). Protein complex prediction with alphafold-multimer. Preprint at bioRxiv.
64. Huang, D.W., Sherman, B.T., and Lempicki, R.A. (2009). Systematic and integrative analysis of large gene lists using DAVID bioinformatics resources. Nat. Protoc. *4*, 44–57.
65. Schindelin, J., Arganda-Carreras, I., Frise, E., Kaynig, V., Longair, M., Pietzsch, T., Preibisch, S., Rueden, C., Saalfeld, S., Schmid, B., et al. (2012). Fiji: an open-source platform for biological-image analysis. Nat. Methods *9*, 676–682.
66. Hess, B., Kutzner, C., van der Spoel, D., and Lindahl, E. (2008). GROMACS 4: Algorithms for Highly Efficient, Load-Balanced, and Scalable Molecular Simulation. J. Chem. Theory Comput. *4*, 435–447.
67. Lindahl, E., Hess, B., and van der Spoel, D. (2001). GROMACS 3.0: a package for molecular simulation and trajectory analysis. J. Mol. Model. *7*, 306–317.
68. Pronk, S., Páll, S., Schulz, R., Larsson, P., Bjelkmar, P., Apostolov, R., Shirts, M.R., Smith, J.C., Kasson, P.M., van der Spoel, D., et al. (2013). GROMACS 4.5: a high-throughput and highly parallel open source molecular simulation toolkit. Bioinformatics *29*, 845–854.
69. Schneider, C.A., Rasband, W.S., and Eliceiri, K.W. (2012). NIH Image to ImageJ: 25 years of image analysis. Nat. Methods *9*, 671–675.
70. Cox, J., Neuhauser, N., Michalski, A., Scheltema, R.A., Olsen, J.V., and Mann, M. (2011). Andromeda: a peptide search engine integrated into the MaxQuant environment. J. Proteome Res. *10*, 1794–1805.
71. Michaud-Agrawal, N., Denning, E.J., Woolf, T.B., and Beckstein, O. (2011). MDAnalysis: a toolkit for the analysis of molecular dynamics simulations. J. Comput. Chem. *32*, 2319–2327.
72. Gowers, R.J., Linke, M., Barnoud, J., Reddy, T.J.E., Melo, M.N., Seyler, S.L., Dotson, D.L., Domanski, J., Buchoux, S., Kenney, I.M., and Beckstein, O. (2016). Beckstein. MDAnalysis: A Python package for the rapid analysis of molecular dynamics simulations (Austin, TX: SciPy), pp. 98–105. https://doi.org/10.25080/majora-629e541a-00e.
73. Tyanova, S., Temu, T., and Cox, J. (2016). The MaxQuant computational platform for mass spectrometry-based shotgun proteomics. Nat. Protoc. *11*, 2301–2319.
74. Harris, C.R., Millman, K.J., van der Walt, S.J., Gommers, R., Virtanen, P., Cournapeau, D., Wieser, E., Taylor, J., Berg, S., Smith, N.J., et al. (2020). Array programming with NumPy. Nature *585*, 357–362.
75. Virtanen, P., Gommers, R., Oliphant, T.E., Haberland, M., Reddy, T., Cournapeau, D., Burovski, E., Peterson, P., Weckesser, W., Bright, J., et al. (2020). SciPy 1.0: fundamental algorithms for scientific computing in Python. Nat. Methods *17*, 261–272.
76. Lee, W., Tonelli, M., and Markley, J.L. (2015). NMRFAM-SPARKY: enhanced software for biomolecular NMR spectroscopy. Bioinformatics *31*, 1325–1327.
77. Baeken, M.W., Weckmann, K., Diefenthaler, P., Schulte, J., Yusifli, K., Moosmann, B., Behl, C., and Hajieva, P. (2020). Novel Insights into the Cellular Localization and Regulation of the Autophagosomal Proteins LC3A, LC3B and LC3C. Cells *9*.
78. Farjon, J., Boisbouvier, J., Schanda, P., Pardi, A., Simorre, J.P., and Brutscher, B. (2009). Longitudinal-relaxation-enhanced NMR experiments for the study of nucleic acids in solution. J. Am. Chem. Soc. *131*, 8571–8577.
79. Williamson, M.P. (2013). Using chemical shift perturbation to characterise ligand binding. Prog. Nucl. Magn. Reson. Spectrosc. *73*, 1–16.
80. Harris, R.K., Becker, E.D., Cabral de Menezes, S.M., Goodfellow, R., and Granger, P. (2002). NMR Nomenclature: Nuclear Spin Properties and Conventions for Chemical Shifts. IUPAC Recommendations 2001. Solid State Nucl. Magn. Reson. *22*, 458–483.
81. Rasmussen, M.S., Birgisdottir, Å.B., and Johansen, T. (2019). Use of Peptide Arrays for Identification and Characterization of LIR Motifs. Methods Mol. Biol. *1880*, 149–161.
82. Kulak, N.A., Pichler, G., Paron, I., Nagaraj, N., and Mann, M. (2014). Minimal, encapsulated proteomic-sample processing applied to copy-number estimation in eukaryotic cells. Nat. Methods *11*, 319–324.
83. Demel, U.M., Böger, M., Yousefian, S., Grunert, C., Zhang, L., Hotz, P.W., Gottschlich, A., Köse, H., Isaakidis, K., Vonficht, D., et al. (2022). Activated SUMOylation restricts MHC class I antigen presentation to confer immune evasion in cancer. J. Clin. Invest. *132*, e152383.
84. McAlister, G.C., Nusinow, D.P., Jedrychowski, M.P., Wühr, M., Huttlin, E.L., Erickson, B.K., Rad, R., Haas, W., and Gygi, S.P. (2014). MultiNotch MS3 enables accurate, sensitive, and multiplexed detection of differential expression across cancer cell line proteomes. Anal. Chem. *86*, 7150–7158.
85. Elias, J.E., and Gygi, S.P. (2007). Target-decoy search strategy for increased confidence in large-scale protein identifications by mass spectrometry. Nat. Methods *4*, 207–214.
86. Herhaus, L., van den Bedem, H., Tang, S., Maslennikov, I., Wakatsuki, S., Dikic, I., and Rahighi, S. (2019). Molecular Recognition of M1-Linked Ubiquitin Chains by Native and Phosphorylated UBAN Domains. J. Mol. Biol. *431*, 3146–3156.
87. Huang J., Rauscher S., Nawrocki G., Ran T., Feig M., de Groot B.L., Grubmueller H., MacKerell A.D. CHARMM36m: An Improved Force Field for Folded and Intrinsically Disordered Proteins. Nat. Methods 14, 71–73 (2017). doi: 10.1038/nmeth.4067. PMID: 27819658
88. Jo, S., Kim, T., Iyer, V.G., and Im, W. (2008). CHARMM-GUI: a web-based graphical user interface for CHARMM. J. Comput. Chem. *29*, 1859–1865.

89. Nosé, S. (1984). A molecular dynamics method for simulations in the canonical ensemble. Mol. Phys. *52*, 255–268. https://doi.org/10.1080/00268978400101201.

90. Nosé, S. (1984). A unified formulation of the constant temperature molecular dynamics methods. J. Chem. Phys. *81*, 511–519. https://doi.org/10.1063/1.447334.

91. Hoover, W.G. (1985). Canonical dynamics: Equilibrium phase-space distributions. Phys. Rev. A *31*, 1695–1697. https://doi.org/10.1103/PhysRevA.31.1695.

92. Parrinello, M., and Rahman, A. (1981). Polymorphic transitions in single crystals: A new molecular dynamics method. J. Appl. Phys. *52*, 7182–7190. https://doi.org/10.1063/1.328693.

STAR★METHODS

KEY RESOURCES TABLE

REAGENT or RESOURCE	SOURCE	IDENTIFIER
Antibodies		
anti-Flag (M2)	Sigma Aldrich	Cat# F1804; RRID: AB_262044
anti-Vinculin	Sigma Aldrich	Cat# V9131; RRID: AB_477628
anti-β-Tubulin (E7)	Developmental Studies Hybridoma Bank	clone E7
anti-B23 (NA24)	Santa Cruz	Cat# sc-53175; RRID: AB_630048
anti-NPM1 (FC-61991)	Invitrogen	Cat# 32–5200; RRID: AB_2533084
anti-p53 (DO-1)	Santa Cruz	Cat# sc-126; RRID: AB_628082
anti-p62	Enzo	Cat# BML-PW9860; RRID: AB_2196009
anti-Histone H3	Abcam	Cat# ab1791; RRID: AB_302613
anti-phopho-ATG14 (Ser29) (D4B8M)	Cell Signaling	Cat# 92340; RRID: AB_2800182
anti-phospho-p70 S6 Kinase (Thr389) (108D2)	Cell Signaling	Cat# 9234; RRID: AB_2269803
anti-Ulk1 (D8H5)	Cell Signaling	Cat# 8054; RRID: AB_11178668
anti-His-Tag Antikörper (AD1.1.10)	Santa Cruz	Cat# sc-53073; RRID: AB_783791
anti-GST (B14)	Santa Cruz	Cat# sc-138; RRID: AB_627677
anti-GABARAPL1-specific	Proteintech	Cat# 11010-1-AP; RRID: AB_2294415
anti-LC3B	Cell Signaling	Cat# 2775; RRID: AB_915950
anti-Lamp1	Abcam	Cat# Ab24170; RRID: AB_775978
Anti-phosphoTFEB(S211)	Cell Signaling	Cat# 37681; RRID: AB_2799117
anti-GABARAP+GABARAPL1+ GABARAPL2 (EPR4805)	Abcam	Cat# ab109364; RRID: AB_10861928
anti-TFEB (D207D)	Cell Signaling	Cat# 37785; RRID: AB_2799119
anti-NPM1c	Thermo Fisher Scientific	Cat# PA1-46356; RRID: AB_2267471
anti-NPM1(all)	Santa Cruz	Cat# sc-53175; RRID: AB_630048
anti-mouse-HRP	Dianova	Cat# 115-035-146
anti-rabbit-HRP	Dianova	Cat# 111-035-045
anti-mouse IgG-IRDye 800CW	LI-COR	Cat# 926–32210; RRID: AB_621842
anti-mouse IgG-IRDye 800CW	LI-COR	Cat# 926–32211; RRID: AB_621843
anti-mouse IgG(H + L)-Alexa Fluor™ 647	Invitrogen	Cat# A-31571

(*Continued on next page*)

Continued

REAGENT or RESOURCE	SOURCE	IDENTIFIER
Anti-rabbit IgG(H + L)-Alexa Fluor™ 488	Invitrogen	Cat# A-21206
Duolink® *In Situ* PLA® Probe Anti-Mouse PLUS	Sigma	Cat# DUO92001
Duolink® *In Situ* PLA® Probe Anti-Rabbit MINUS	Sigma	Cat# DUO92005
Bacterial and virus strains		
BL21 *E. coli*	Stratagene	N/A
NEB T7 express competent *E.coli* cells	New England Biolabs	N/A
Chemicals, peptides, and recombinant proteins		
Acetonitrile	Sigma Aldrich	34851
Ampicillin, sodium salt	Carl-Roth	K029.3
Aprotinin	Carl-Roth	A162.2
Bafilomycin A1	Tocris	S1413
Benzonase	Millipore	70756
Bromphenol blue	Carl Roth	A512.1
BSA	Carl Roth	8076.2
Calcium chloride (CaCl2 2.H2O)	Carl-Roth	5239.2
Cell culture microplate with μclear flat bottom	Greiner	655090
Coomassie brilliant blue G250	Carl-Roth	9598.2
Coverslips (0,17 ± 0.005 mm)	Carl-Roth	LH23.1
Cycloheximide	VWR	441892A
di-Sodium hydrogen phosphate dihydrate (Na2HPO4 · 2 H2O)	Carl-Roth	4984.3
DMEM high glucose	Gibco	41966
DMP	Thermo Fisher Scientific	21667
DMSO	Applichem	A3672
Doxycyclinehyclate	Fluka	44577
dTAG-13	bio-techne	6605
DTT	Carl-Roth	6908.2
Duolink® *In Situ* Wash Buffers, Fluorescence	Sigma	DUO82049-4L
EBSS	Gibco	24010
EDTA	Honeywell/Fluka	34549
Fetal bovine serum	Sigma	F7524
Formic acid	Merck KGaA	33015-M
Fugene® HD Transfection Reagen	Promega	E2311
Glycerol 99% p. a	Carl-Roth	7530.4
H3BO3 Boric Acid	Carl-Roth	6943.1
High Pure RNA isolation kit	Roche	11828665001
Imidazole (BioUltra, ≥99.5% (GC)	Sigma Aldrich	56749-1kg
InstantBlue	expedeon	ISB1L
Isopropyl β-D-1-thiogalactopyranoside (IPTG)	Carl-Roth	2316.5
KOH	Carl Roth	6751.3
Leupeptin Hemisulfate	Applichem	A2183,0025
Lipofectamine RNAiMAX Transfection Reagent	Thermo Fisher Scientific	13778150
LysoTracker red DND 99	Invitrogen	L7528
Lysysl Endopeptidase (LysC)	Wako	129–02541
Magnesium chloride	Sigma Aldrich	M8266
Magnesium chloride (MgCL2 6.H2O)	Carl-Roth	2189.2
Magnesium sulfate (MgSO4 7.H2O)	Carl-Roth	P027.2
Manganese(II)chloride tetrahydrate (MnCl2 · 4 H2O)	Carl-Roth	T881.1
MG132	Selleckchem	S2619

(*Continued on next page*)

Continued

REAGENT or RESOURCE	SOURCE	IDENTIFIER
N-2-Hydroxyethylpiperazine-N′-2-ethane sulphonic acid (HEPES) ≥99.5% p.a.	Carl-Roth	9105.5
NaOH	Applichem	1.316.871.211
Nickel(II) sulfate hexahydrate (NiSO4 · 6 H2O)	Carl-Roth	T111.2
NP-40	Applichem	A1694.0250
NPM1$^{1-20}$: MEDSMDMDMSPLRPQNYLFG	GenScript	N/A
NPM1$_{5A}$$^{1-20}$: MEASADAAASPLRPQNYLFG	GenScript	N/A
NucBlue™ Live ReadyProbes™ Reagent (Hoechst 33342)	Thermo Fisher Scientific	R37605
Pepstatin A	Carl-Roth	2936.2
Peptone from casein, tryptic digest	Carl-Roth	8986.4
PhosSTOP EASYpack	Roche	4906845001
Pierce™ Anti-HA Magnetic Beads	Thermo Fisher Scientific	88836
Pierce™ magnetic Anti-DYKDDDDK-Agarose	Thermo Fisher Scientific	A36797
PMSF	Carl-Roth	6367.1
Ponceau S	Carl-Roth	5938.2
Potassium dihydrogen phosphate (KH2PO4)	Carl-Roth	3904.1
Precision Plus Protein Dual Color Standards	Bio-Rad Laboratories GmbH	1610374
ProLong Gold Antifade Mountant	Thermo Fisher Scientific	P36930
Protino Glutathione Agarose 4B beads	Machery-Nagel	64-17-5
Protino Ni-NTA Agarose beads	Machery-Nagel	745400
Puromycin	Carl Roth	0240.3
QPCR SYBRGreen Master Mix	Steinbrenner	SL-9902
Revert 700 Total Protein Stain	LI-COR	926–11011
RPMI1640	GIBCO	11530586
SDS	Carl Roth	CN30.3
Sequencing Grade Modified Trypsin	Promega	V511C
Sodium Chloride	Carl-Roth GmbH	0601.2
TEV Protease	Prepared by Dr. Jakob Gebel	N/A
Thiamin hydrochloride	Sigma	T1270-25G
Thiourea	Applichem	1.417.431.210
TMTpro™ 16plex reagent	Thermo	A44520
Torin 1	Tocris	4247
Transcriptor First Strand cDNA Synthesis Kit	Roche	04897030001
Trichloroacetic acid	Sigma Aldrich	91228
Tris-(2-carboxyethyl)-phosphine hydrochloride (TCEP)	Carl-Roth GmbH	HN95.3
Tris-(hydroxymethyl)-aminomethane (TRIS)	Carl-Roth GmbH	4855.3
Triton X-100	Carl Roth	3051.2
Trypsin EDTA solution	Pan Biotech	P10-023100
Urea	Applichem	A1049.1000
Yeast extract, micro-granulated	Carl-Roth GmbH	2904.5
Zinc chloride (ZnCl2)	Carl-Roth GmbH	T887.1
Critical commercial assays		
Duolink® *In Situ* Detection Reagents Red	Sigma	DUO92008
Deposited data		
HA-GABARAPL1 immunoprecipitation with siRNA-mediated NPM1 depletion	PRIDE	PRIDE: PXD040220
Whole cell proteome of OCI-AML3 FKBP12(F36V) cells with dTAG-13 treatment	PRIDE	PRIDE: PXD045357

(*Continued on next page*)

Continued

REAGENT or RESOURCE	SOURCE	IDENTIFIER
Whole cell proteome of U-2 OS cells with NPM1 and NPM1c overexpression	PRIDE	PRIDE: PXD040193
Experimental models: Cell lines		
Hel276 $^{GFP-LC3B-mCherry}$	Koschade et al.[22]	N/A
HeLa	ATCC (CCL-2)	RRID: CVCL_0030
MV4-11 $^{GFP-LC3B-mCherry}$	Koschade et al.[22]	N/A
OCI-AML2	Leibniz-Institut DSMZ	RRID: CVCL_1619
OCI-AML3	Leibniz-Institut DSMZ	RRID: CVCL_1844
OCI-AML3$^{GFP-LC3B-mCherry}$	Koschade et al.[22]	N/A
OCI-AML3$^{NPM1c-FKBP12(F36V)\ -P2A-GFP}$	Brunetti et al.[34]	N/A
U-2 OS	ATCC (HTB-96)	RRID: CVCL_0042
U-2 OS$^{GFP-LC3B-RFP-LC3B\Delta G}$	Hertel et al.[58]	N/A
U-2 OS$^{GFP-mCherry-LC3B}$	Gift from Ivan Dikic	N/A
Oligonucleotides		
GABARAPL1 for 5′ (AGGAGGACCATCCCTTTGAGT) 3′	Eurofins	N/A
GABARAPL1 rev 5′ (TGGCCAACAGTAAGGTCAGA) 3′	Eurofins	N/A
GAPDH for 5′ (TCGGAGTCAACGGATTTG) 3′	Eurofins	N/A
GAPDH rev 5′ (CAACAATATCCACTTTACCAGAG) 3′	Eurofins	N/A
MISSION® siRNA Universal Negative Control #2	Merck	SIC002
siATG5: 5′ (GGAAUAUCCUGCAGAAGAA)TT 3‘	Eurofins	N/A
sigl2: 5′ (CGUACGCGGAAUACUUCG A)TT 3’	Eurofins	N/A
siNPM1_UTR: 5′ (CCTACCGTGTTTGATAAAT)TT 3′	Eurofins	N/A
siNPM1: 5′ (GGAAGUCUCUUUAAGAAAA)TT 3′	Eurofins	N/A
siNPM1c: 5′ (CTCTGTCTGGCAGTGGAGGAA)TT 3′	Eurofins	N/A
Recombinant DNA		
pcDNA3.1-HA-GABARAPL1	Provided by I. Dikic	N/A
pCI	Promega	E1731
pCI-Flag-NPM1	Haindl et al.[59]	N/A
pCI-Flag-NPM1$^{1-117}$	This Study	N/A
pCI-Flag-NPM1$^{1-189}$	This Study	N/A
pCI-Flag-NPM1$^{11-294}$	This Study	
pCI-Flag-NPM1$^{118-294}$	This Study	N/A
pCI-Flag-NPM1c	This Study	N/A
pCI-Flag-NPM1c$^{11-298}$	This Study	N/A
pET28-His-NPM1$^{1-117}$	This Study	N/A
pET28-His-NPM1$^{11-117}$	This Study	N/A
pET28-His-NPM1$^{15-117}$	This Study	N/A
pET28-His-NPM1$_{5A}^{1-117}$	This Study	N/A
pET53-His-GABARAPL1	Provided by I. Dikic	N/A
pETm60-Ubiquitin3-His-TEV-GABARAPL1$^{2-117}$	Rogov et al.[39]	N/A
pETm60-Ubiquitin3-His-TEV-NPM1$^{1-117}$	This study	N/A
pETm60-Ubiquitin3-His-TEV-NPM1$_{5A}^{1-117}$	This study	N/A
pETm60-Ubiquitin3-His-TEV-NPM1$_{5A}^{fl}$	This study	N/A
pETm60-Ubiquitin3-His-TEV-TEV-NPM1^{fl}	This study	N/A
pGEX-4T1-NPM1	This Study	N/A
pGEX4T1	GE-Healthcare	28-9545-49
pGEX4T1-hGABARAP(ΔG)	Kirkin et al.[60]	N/A
pGEX4T1-hGABARAPL1(ΔG)	Kirkin et al.[60]	N/A
pGEX4T1-hGABARAPL1(ΔG)^{F77A}	This study	N/A

(*Continued on next page*)

Continued

REAGENT or RESOURCE	SOURCE	IDENTIFIER
pGEX4T1-hGABARAPL1(ΔG)^{V51A}	This study	N/A
pGEX4T1-hGABARAPL1(ΔG)^{V51A,F60A}	This Study	N/A
pGEX4T1-hGABARAPL2 (GATE-16)(ΔG)	Kirkin et al.[60]	N/A
pGEX4T1-hMAP1LC3B(ΔG)	Kirkin et al.[60]	N/A
pRTS	Bornkamm et al.[61]	N/A
pRTS-Flag-NPM1	Haindl et al.[59]	N/A
pRTS-Flag-NPM1c	This Study	N/A
pRTS-Flag-NPM1c$^{11-298}$	This Study	N/A
pRTS-Flag-NPM1wt$^{11-294}$	This Study	N/A
Software and algorithms		
AlphaFold	Jumper et al.[62], Evans et al.[63]	https://github.com/deepmind/alphafold
BioVoxxel	J. Brocher	https://github.com/biovoxxel/BioVoxxel-Toolbox/tree/v2.5.3
CellProfiler 4.2.1	Broad Institute, Cambridge, Massachusetts, USA	https://cellprofiler.org
CQ1 Software	Yokogawa	https://www.yokogawa.com/de/library/documents-downloads/software/lsc-cq1-software/
DAVID	Huang et al.[64]	https://david.ncifcrf.gov
Fiji for ImageJ	Schindelin et al.[65]	https://ImageJ.net/Fiji
FlowJo™ Software, Version 10.4.2	Becton, Dickinson and Company	https://www.flowjo.com
GraphPad Prism, version 5.0b for MAC OS X	GraphPad Software, La Jolla California USA	www.graphpad.com
GROMACS (version 2021.5)	Hess et al., Lindahl et al., Pronk et al.[66–68]	https://www.gromacs.org
ImageJ, version 2.0.0-rc-69/1.52n	Schneider et al.[69]	https://ImageJ.net
Maxquant, version 1.6.17.0	Cox et al.[70]	https://www.biochem.mpg.de/5111795/maxquant
MDAnalysis	Michaud-Agrawal et al.[71], Gowers et al.[72]	https://www.mdanalysis.org
Origin 2018	Origin, Version 2018. OriginLab Corporation, Northampton, MA, USA.	www.originlab.com
Perseus, version 1.6.15.0	Tyanova et al.[73]	https://www.biochem.mpg.de/5111810/perseus
Proteome Discoverer 2.4	Thermo Fisher Scientific	https://www.thermofisher.com/de/de/home/industrial/mass-spectrometry/liquid-chromatography-mass-spectrometry-lc-ms/lc-ms-software/multi-omics-data-analysis/proteome-discoverer-software.html
Python3 (NumPy, SciPy)	Harris et al.[74], Virtanen et al.[75]	https://www.python.org
R Studio, version 2021.09.2 “Ghost Orchid”	RStudio: Integrated Development for R. RStudio, Inc.	https://www.rstudio.com
SPARKY	Lee et al.[76]	https://www.cgl.ucsf.edu/home/sparky/
TopSpin	TopSpin	www.bruker.com; RRID: SCR_014227

RESOURCE AVAILABILITY

Lead contact

Further information and requests for resources and reagents should be directed to and will be fulfilled by the Lead Contact, Stefan Müller (ste.mueller@em.uni-frankfurt.de).

Materials availability

Plasmids and other materials generated in this study are available upon request.

Data and code availability

- Data availability: Mass spectrometry proteomics data have been deposited to the ProteomeXchange Consortium via the PRIDE partner repository with the dataset identifiers listed in the key resources table.
- Code availability: This paper does not report original code.
- Any additional information required to reanalyze the data reported in this paper is available from the lead contact upon request.

EXPERIMENTAL MODEL AND STUDY PARTICPANT DETAILS

HEK 293T and U-2 OS cells (ATCC) were cultured in Dulbecco's Modified Eagle Medium (DMEM) (Thermo Fisher Scientific) supplemented with 10% fetal calf serum (Thermo Fisher Scientific), 100 U/ml penicillin, and 100 U/ml streptomycin (Thermo Fisher Scientific) at 37°C and 5% CO_2. U-2 OS cells with stable expression of GFP-mCherry-LC3B (U-2 OS$^{GFP\text{-}mCherry\text{-}LC3B}$) were provided by Prof. Ivan Dikic, and GFP-LC3B-RFP-LC3BΔG (U-2 OS$^{GFP-LC3B-RFP\text{-}LC3B\Delta G}$) were provided by Dr. Anja Bremm and have been described before.[58] AML cell lines (OCI-AML2, OCI-AML3, MV4-11, and Hel276) were cultured in RPMI1640 medium (Thermo Fisher Scientific) supplemented with 10% fetal calf serum, 100 U/ml penicillin, and 100 U/ml streptomycin at 37°C and 5% CO_2. The AML cell lines with the GFP-LC3B-RFP reporter (Hel276 $^{GFP-LC3B-mCherry}$, MV4-11 $^{GFP-LC3B-mCherry}$, and OCI-AML3$^{GFP-LC3B-mCherry}$) were generated and provided by Dr. Sebastion Koschade and the NPM1c-FKBP expressing OCI-AML3 cells (OCI-AML3$^{NPM1c-FKBP12(F36V)\text{-}P2A-GFP}$) by Dr. Lorenzo Brunetti as described before.[22,34]

METHOD DETAILS

Transfection and treatment of cell lines

For the conditional expression system with the pRTS1 episomal expression plasmid [59,60], U-2 OS cells were transfected with FuGene and after 24 h selected with 400 μg/mL hygromycin for 11 days. If not stated differently, expression was induced for 24 h with 0.1 μg/mL doxycycline. For transient overexpression, HEK 293T cells were transfected with plasmid DNA for 48 h using the Calcium Phosphate Transfection method with HEPES buffered saline. For gene knockdown of adherent cells, Lipofectamine RNAiMAX transfection reagent (Thermo Fisher Scientific) was used to transfect gene-specific siRNAs for 72 h. AML cell lines were transfected with siRNA using the 100 μL Kit of the Neon Electroporation system (Invitrogen) according to the manufacturer's instructions. 2 Million cells were used per electroporation with the following conditions: 1350 V, 35 ms, and 1 pulse. Cells were harvested after 72 h.

When indicated, cells were exposed to amino acid starvation by changing the media with extensive washing to EBSS (Earle's balanced salt solution; Gibco) for 30 min to 4 h. Treatment with Bafilomycin A1, Torin 1, Cyclohexemide, and MG132 was done for the indicated time points.

GST pulldown and *in vitro* interaction

HEK cells with or without transfection of NPM1 variants are scraped in GST buffer (50 mM Tris pH 7.5, 150 mM NaCl, 10 mM EDTA. 5 mM EGTA, 1 mM DTT, 1 mM PMSF, 2 μg/mL Aprotinin, 2 μg/mL Leupeptin, 1 μg/mL Pepstatin A and 1x PhosStop (Roche)) supplemented with 1% NP-40, rotated for 1 h at 4°C and homogenized with an insulin needle. Debris was separated by centrifugation at 12000x g for 15 min. For each pull-down, 0.5–1 mg of HEK cell lysate was diluted with GST buffer to 0.5% NP40 and incubated with GST proteins immobilized on GSH beads. For the *in vitro* interaction experiments, His-tagged NPM1 variants were incubated with the GST proteins immobilized on GSH beads in GST buffer containing 0.2% NP40 in the presence or absence of fresh HEK cell lysate. After rotation for 2 h at 4°C, the beads were washed three times with GST buffer containing 0.1% NP-40 and boiled in 2x Laemmli buffer (20.8mM Tris (pH 6.8), 3.3% glycerol, 0.67% SDS, 1.67% β-mercaptoethanol, 0.0033% bromophenol blue).

Cycloheximide chase experiment

U-2 OS cells expressing doxycycline-inducible (Tet-On) Flag-NPM1 variants were treated with Cyclohexemide for the indicated time points in EBSS or fresh culture media. The samples were scraped in 50 mM Tris (pH 8.5) with 2% SDS and were directly boiled in 1x Laemmli buffer.

Subcellular fractionation

Subcellular Fractionation of U-2 OS cells expressing doxycycline-inducible Flag-NPM1 variants was performed as previously described.[77] In brief, U-2 OS cells were washed in PBS and scraped in fractionation buffer (20 mM HEPES, pH 7.4; 250 mM sucrose; 10 mM KCl; 1.5 mM $MgCl_2$; 1 mM EDTA; 1 mM EGTA; 1 mM PMSF, 2 μg/mL Aprotinin, 2 μg/mL Leupeptin, and 1 μg/mL Pepstatin A), passed through a 25-gauge needle and left on ice for 20 min. Nuclei were isolated through centrifugation at 720*g* for 10 min at 4°C and washed once in fractionation buffer and then resuspended in fractionation buffer. Both whole cell lysate and nuclei were

supplemented with a final concentration of 2% SDS and boiled for 5 min. Protein concentrations were determined using the Lowry technique, and equal amounts were boiled in 1x Laemmli sample buffer.

Cell lysis and immunoblotting

Unless described differently, cells were lysed in RIPA buffer. For expression, control cells were directly lysed and boiled in 2x Laemmli buffer. Protein samples were separated by SDS-PAGE and transferred to NC membranes in Towbin buffer containing 20% methanol. Membranes were blocked in 5% (w/v) milk powder in PBST before the primary antibody was added overnight in a blocking buffer (4°C). After extensive washing with PBST, membranes were incubated with horseradish peroxidase (HRP)-coupled or fluorescently labeled secondary antibodies for 1 h in blocking buffer at RT, followed by extensive washing. The fluorescence signal for membranes incubated with fluorescently labeled secondary antibodies was determined using the LI-COR system (Odyssey CLx Imager). Membranes with HRP-coupled antibodies were incubated for 1 min with Immobilon ECL Ultra Western HRP Substrate (Merck-Millipore) and developed with Super RX-N films (Fujifilm) in a CURIX 60 developer machine (Agfa). If shown, membranes were stained and imaged with Ponceau S solution or Revert 700 Total Protein Stain (Li-COR) before blocking. All displayed Western Blots are representative examples.

Protein expression and purification

His- or GST-tagged proteins were expressed in transformed BL21 *E. coli* cells with 0.5 μM IPTG overnight (17°C). After centrifugation, the bacteria pellet was lysed in GST protein purification buffer (1x PBS, 1% (v/v) Triton X-100, 1 mM DTT, 1 mM PMSF) or His protein purification buffer (50 mM NaH_2PO_4, 50 mM NaCl, 1% Triton X-100 10 mM Imidazole, 1 mM PMSF, pH 8). For complete lysis, cells were subjected to repeated freeze-thaw cycles and sonification. All further steps are performed at 4°C. The lysates were cleared from cell debris by centrifugation (60 min, 25000g), and the supernatant was incubated with Protino Glutathione Agarose 4B beads (Machery-Nagel) in case of GST-proteins or Protino Ni-NTA Agarose beads (Machery-Nagel) in case of His-proteins. After rotation for 2 h, beads were washed 4 times with GST- or His-protein purification buffer. The purified proteins were either stored on beads in PBS supplemented with 10% DMSO at −20°C or eluted two times for 30 min with 10 mM Glutathione in 50 mM Tris (pH 8) in case of GST proteins or 250 nM Imidazole in His protein purification buffer in case of His proteins. Eluted proteins were subjected to dialysis in PBS with a 3 kDa cutoff. Eluted proteins were directly used for a subsequent experiment.

Ubiquitin3-His-TEV-$NPM1^{fl}$, -$NPM1_{5A}^{fl}$, -$NPM1^{1-117}$, and -$NPM1_{5A}^{1-117}$ were expressed in transformed BL21 *E. coli* cells with 0.5 μM IPTG overnight (17°C). Cells were harvested by centrifugation, resuspended in IMAC A buffer (50 mM Tris, 200 mM NaCl, 25 mM Imidazole, 20 mM β-mercaptoethanol, pH 7.5) supplemented with self-made protease inhibitor cocktail, and lysed by sonification. All further steps were performed at 4°C. The lysate was cleared by centrifugation (17,000 rpm, 45 min), and the supernatant was loaded onto a pre-equilibrated immobilized metal affinity chromatography (IMAC) column (HisTrap IMAC Sepharose FF, Cytiva). The loaded column was washed with IMAC A buffer to 5 column volume (CV). Bound His-tagged proteins were eluted with IMAC A buffer supplemented with 400 mM imidazole (IMAC B). N-terminal HIS-tag of the eluted protein was cleaved with 1 mg in-house purified TEV protease per 50 mg of protein during dialysis in IMAC A buffer, using 3.5 kDa cutoff dialysis membrane (Spectrum Labs, Inc.), overnight at 4°C. Dialyzed (cleaved) proteins were subjected to reverse IMAC. The flow-through containing the cleaved proteins of interest was collected and concentrated using 30 kDa and 10 kDa cutoff Amicon Ultra Centrifugal Filters (Millipore) for $NPM1^{fl}$ or $NPM1_{5A}^{fl}$ and $NPM1^{1-117}$ or $NPM1_{5A}^{1-117}$, respectively. The concentrated proteins were further purified and subjected to a buffer exchange by size exclusion chromatography (SEC) with SEC buffer (25 mM HEPES, NaCl 100 mM, TCEP 0.5 mM, pH 7.5) using a HiLoad Superdex 75 16/60 self-packed column (Cytiva) on the AKTA purifier FPLC system (GE Healthcare Europe GmbH). Central peak fractions were collected and concentrated to the desired concentration with the respective Amicon filter. The purity and molecular size of the purified proteins were monitored by SDS-PAGE with Coomassie staining. Proteins were flash-frozen in liquid nitrogen prior to storage at −80°C until further use.

To prepare ^{15}N-GABARAPL1, Ubiquitin3-His-TEV-$GABARAPL1^{2-117}$ was expressed in transformed T7 *E. coli* cells with 1 μM IPTG overnight (20°C) in M9 minimal media. The purification was performed as described above for $NPM1^{1-117}$ and $NPM1_{5A}^{1-117}$.

Nuclear magnetic resonance (NMR) spectroscopy

Proteins for NMR were purified from *E.coli* as described before, and NPM1 peptides ($NPM1^{1-20}$: MEDSMDMDMSPLRPQNYLFG and $NPM1_{5A}^{1-20}$: MEASADAAASPLRPQNYLFG) were purchased from GenScript. NMR samples contained ^{15}N-GABARAPL1 at 55 μM initial concentration in SEC buffer, supplemented with 5% D_2O and 1 mM Imidazole, for pH control.

All spectra were recorded at the sample temperature of 25°C using the Bruker AV III HD 700 MHz spectrometer equipped with cryogenic 1H{^{31}P/^{13}C/^{15}N} QCI probe in case of $NPM1^{1-20}$ and $NPM1_{5A}^{1-20}$, or using the Bruker AvanceNeo 600 MHz spectrometer equipped with cryogenic 1H{^{13}C/^{15}N} TCI probe in case of $NPM1^{1-117}$ and $NPM1_{5A}^{1-117}$, or using the Bruker AVIIIHD 800 MHz spectrometer equipped with cryogenic 1H{^{13}C/^{15}N} TCI probe in case of $NPM1^{fl}$ and $NPM1_{5A}^{fl}$. ^{15}N-GABARAPL1 was titrated with purified NPM1 constructs to obtain the ratio of 1:5, 1:10 and 1:15 for recording spectra. Proton nitrogen correlation spectra were obtained using the BEST-TROSY pulse sequence, and chemical shift perturbation (CSP) was calculated as described before using SPARKY.[78,79] Chemical shifts are referenced to sodium trimethylsilylpropanesulfonate (DSS) as an internal standard.[80]

Peptide array

A modified cellulose SPOT membrane containing 20-mer peptides of NPM1$^{1-189}$ in duplicates was purchased from Intavis Peptide Services. Incubation with purified GST or GST-GABARAPL1 protein was performed according to Rasmussen et al.[81] Quantification of the signals was done in ImageJ. The intensities of the GST-GABARAPL1 signals were normalized to the GST signals in Excel and visualized in GraphPad Prism.

qRT-PCR

Total RNA from U-2 OS cells expressing doxycycline-inducible Flag-NPM1 variants was isolated using the High Pure RNA isolation kit (Roche). For cDNA synthesis, 500 ng total RNA was transcribed with the Transcriptor First Strand cDNA Synthesis Kit (Roche) using the Poly-dT Primer. RT-qPCR was performed with the QPCR SYBRGreen Master Mix (Steinbrenner) and gene-specific primers for GABARAPL1 or *GAPDH* using the LightCycler 480 II (Roche). Ct values were calculated with the LightCycler 480 Software 1.5.0 SP4 (Roche) and normalized to GAPDH gene expression with the delta-delta Ct ($2^{-\Delta\Delta Ct}$) method in Excel. Statistical analysis and visualization were done in GraphPad Prism. For each biological replicate, at least three technical replicates were measured.

Immunoprecipitation and sample preparation

For HA-immunoprecipitation (IP), HEK cells transiently expressing HA-GABARAPL1 with NPM1 or Contr knockdown or non-transfected MOCK control cells were treated for 2 h with 200 nM Bafilomycin A1 before scraping in IP lysis buffer (20 mM Tris, 150 mM NaCl, 0.5% Triton, 10% Glycerol, 1x PhosStop (Roche), 1 mM PMSF, 2 μg/mL Aprotinin, 2 μg/mL Leupeptin, 1 μg/mL Pepstatin A, 28U/μL Benzonase (Millipore), and 1x PhosStop (Roche)). For Flag-IP, HEK cells transiently expressing Flag-NPM1, -NPM1c, -NPM1$^{11-294}$, or -NPM1c$^{11-298}$ and MOCK control cells were scraped in IP lysis buffer. All the following steps were performed at 4°C. The lysate was rotated for 1 h, homogenized with an insulin needle and debris was separated by centrifugation at 12000x g for 15 min. For each sample, 1 mg of cell lysate was incubated overnight with 15 μL Pierce Anti-HA Magnetic Beads (Thermo) or Pierce magnetic Anti-DYKDDDDK-Agarose on a rotating wheel. The next day, the beads were washed three times with IP buffer and one time with 50 mM Tris before elution with 2% sodium deoxycholate (SDC) in 50 mM Tris (pH 8.5) at 95°C for 5 min. For mass spectrometry sample preparation, the eluted proteins were reduced and alkylated by adding 1 mM TCEP and 4 mM chloroacetamide for 5 min at 95°C. After diluting the samples to 1% SDC in 50 mM Tris (pH 8.5), 500 ng Trypsin and 500 ng LysC were added overnight at 37°C to digest the sample. The digestion was stopped with the addition of 0.25% trifluoroacetic acid (TFA), and peptides were cleaned up using styrene-divinyl benzene reverse phase sulfonate (SDB-RPS) polymer sorbent Solid phase extraction StageTips according to Kulak et al.[82] Peptides were dried in a vacuum concentrator and resuspended in 2% acetonitrile (ACN) and 0.1% TFA for LC-MS analysis. IPs were performed in triplicates and processed in parallel.

Sample preparation for the whole cell proteome

U-2 OS cells expressing doxycycline-inducible Flag-NPM1wt or c were washed with PBS and scraped in lysis buffer (2% SDS, 50 mM Tris/HCl, 10 mM TCEP, 40 mM CAA, 1 mM PMSF, 2 μg/mL Aprotinin, 2 μg/mL Leupeptin, 1 μg/mL Pepstatin A, pH 8.5). OCI-AML3 FKBP12(F36V) cells with dTAG-13 treatment were pelleted by centrifugation, washed in PBS and subsequently resuspended in lysis buffer (see above). The samples were prepared in four replicates as described previously.[83] In brief, 50 μg of Methanol-Chloroform precipitated proteins were digested with Trypsin and LysC. For isobaric labeling, 10 μg of desalted peptides were supplemented with 25 μg of the respective TMTpro 16plex reagent (Thermo). The samples were tested for sufficient labeling efficiency and pooled by adjustment to the TMT intensity signal from the test shot. The pooled sample was desalted by SepPak (tC18, 50mg, Waters), and peptides were fractionated using high-pH liquid-chromatography on a micro-flow HPLC (Dionex U3000 RSLC, Thermo Scientific). For that, 45 μg of pooled and purified TMT labeled peptides resuspended in Solvent A (5mM ammonium-bicarbonate, 5%ACN) were separated on a C18 column (XSelect CSH, 1 mm × 150 mm, 3.5 μm particle size; Waters) using a multistep gradient from 3 to 60% Solvent B (5mM ammonium-bicarbonate, 90% ACN) over 65 min at a flow rate of 30 μL/min. Eluting peptides were collected every 43 s from minute 2 for 69 min into a total of 96 fractions, which were cross-concatenated into 24 fractions. Pooled fractions were dried in a vacuum concentrator and resuspended in 2% ACN and 0.1% TFA for LC-MS analysis.

Liquid chromatography and mass spectrometry

Tryptic peptides of the immunoprecipitations were analyzed on a Q Exactive HF coupled to an easy nLC 1200 (ThermoFisher Scientific) using a 35 cm long, 75μm ID fused-silica column packed in-house with 1.9 μm C18 particles (Reprosil pur, Dr. Maisch), and kept at 50°C using an integrated column oven (Sonation). Peptides were eluted by a non-linear gradient from 4 to 28% acetonitrile over 60 min and directly sprayed into the mass-spectrometer equipped with a nanoFlex ion source (ThermoFisher Scientific). Full scan MS spectra (350–1650 m/z) were acquired in Profile mode at a resolution of 60,000 at m/z 200, a maximum injection time of 20 ms, and an AGC target value of 3 x 10^6 charges. Up to 10 most intense peptides per full scan were isolated using a 1.4 Th window and fragmented using higher energy collisional dissociation (normalized collision energy of 27). MS/MS spectra were acquired in centroid mode with a resolution of 30,000, a maximum injection time of 54 ms, and an AGC target value of 1 x 10^5. Single-charged ions, ions with a charge state above 5, and ions with unassigned charge states were not considered for fragmentation, and dynamic exclusion was set to 20s.

Tryptic peptides of the whole cell proteome of U-2 OS cells were analyzed on an Orbitrap Lumos coupled to an easy nLC 1200 (ThermoFisher Scientific) using a 35 cm long, 75μm ID fused-silica column packed in-house with 1.9 μm C18 particles (Reprosil pur, Dr. Maisch), and kept at 50°C using an integrated column oven (Sonation). HPLC solvents consisted of 0.1% Formic acid in water (Buffer A), and 80% acetonitrile in water (Buffer B). Assuming equal amounts in each fraction, 400 ng of peptides were eluted by a non-linear gradient from 7 to 40% Buffer B over 90 min, followed by a stepwise increase to 90% Buffer B in 6 min, which was held for another 9 min. A synchronous precursor selection (SPS) multi-notch MS3 method was used to minimize ratio compression, as previously described (McAlister et al., 2014). Full scan MS spectra (350–1400 m/z) were acquired with a resolution of 120,000 at m/z 200, maximum injection time of 100 ms, and AGC target value of 4×10^5. The most intense precursors with a charge state between 2 and 6 per full scan were selected for fragmentation (''Top Speed'' with a cycle time of 1.5 s) and isolated with a quadrupole isolation window of 0.7 Th. MS2 scans were performed in the Ion trap (Turbo) using a maximum injection time of 50ms, AGC target value of 1.5×10^4, and fragmented using CID with normalized collision energy (NCE) of 35%. SPS-MS3 scans for quantification were performed on the 10 most intense MS2 fragment ions with an isolation window of 0.7 Th (MS) and 2 m/z (MS2). Ions were fragmented using HCD with an NCE of 50% and analyzed in the Orbitrap with a resolution of 50,000 at m/z 200, scan range of 100–500 m/z, AGC target value of 1.5×10^5, and a maximum injection time of 86 ms. Repeated sequencing of already acquired precursors was limited by setting a dynamic exclusion of 60 s and 7 ppm and advanced peak determination was deactivated. All spectra were acquired in centroid mode.

Tryptic peptides of the whole cell proteome of OCI-AML3$^{NPM1c-FKBP12}$ cells were analyzed on an Orbitrap Ascend coupled to a VanquishNeo (ThermoFisher Scientific) using a 25 cm long, 75μm ID fused-silica column packed in house with 1.9 μm C18 particles (Reprosil pur, Dr. Maisch), and kept at 50°C using an integrated column oven (Sonation). HPLC solvents consisted of 0.1% Formic acid in water (Buffer A) and 0.1% Formic acid and 80% acetonitrile in water (Buffer B). Assuming equal amounts in each fraction, 400 ng of peptides were eluted by a non-linear gradient from 7 to 40% B over 90 min, followed by a stepwise increase to 90% B in 6 min, which was held for another 9 min. A synchronous precursor selection (SPS) multi-notch MS3 method was used to minimize ratio compression as previously described.[84] Full scan MS spectra (350–1400 m/z) were acquired with a resolution of 120,000 at m/z 200, maximum injection time of 100 ms, and AGC target value of 4×10^5. The most intense precursors with a charge state between 2 and 6 per full scan were selected for fragmentation (''Top Speed'' with a cycle time of 1.5 s) and isolated with a quadrupole isolation window of 0.7 Th. MS2 scans were performed in the Ion trap (Turbo) using a maximum injection time of 35ms, AGC target value of 10000, and fragmented using CID with a normalized collision energy (NCE) of 35%. SPS-MS3 scans for quantification were triggered only after a successful Real-time search against the human canonical reference proteome from SwissProt with the same search parameter as stated below for data processing in Proteome Discoverer. Criteria for passing the search were Xcorr: 2, dCn: 0.05, and precursor mass accuracy: 10 ppm. Maximum search time was 40ms, and peptide close-out was set to 3 peptides per protein. MS3 acquisition was performed on the 10 most intense MS2 fragment ions with an isolation window of 0.7 Th (MS) and 2 m/z (MS2). Ions were fragmented using HCD with an NCE of 55% and analyzed in the Orbitrap with a resolution of 45,000 at m/z 200 scan range of 100–500 m/z, AGC target value of 150000 and a maximum injection time of 91 ms. Repeated sequencing of already acquired precursors was limited by setting a dynamic exclusion of 60 s and 7 ppm, and advanced peak determination was deactivated. All spectra were acquired in centroid mode.

Mass spectrometry data processing

MS raw data processing of the immunoprecipitations was performed with MaxQuant (v 1.6.17.0) and its in-build label-free quantification algorithm MaxLFQ applying default parameters.[73] Acquired spectra were searched against the human reference proteome (Taxonomy ID 9606) downloaded from UniProt (17-April-2022; ''One Sequence Per Gene'', 20509 sequences) and a collection of common contaminants (244 entries) using the Andromeda search engine integrated into MaxQuant.[70] Identifications were filtered to obtain false discovery rates (FDR) below 1% for both peptide spectrum matches (PSM; minimum length of 7 amino acids) and proteins using a target-decoy strategy.[85]

MS raw data of the proteomes were analyzed with Proteome Discoverer 2.4 (ThermoFisher Scientific). Acquired MS2-spectra were searched against the human reference proteome (Taxonomy ID 9606) downloaded from UniProt (17-April-2022; ''One Sequence Per Gene'', 20509 sequences) and a collection of common contaminants (244 entries from MaxQuant's ''contaminants. fasta'') using SequestHT, allowing a precursor mass tolerance of 7 ppm and a fragment mass tolerance of 0.5 Da after recalibration of mass errors using the Spectra RC-node applying default settings. In addition to standard dynamic (Oxidation on methionines and acetylation of protein N-termini) and static (Carbamidomethylation on cysteines) modifications, TMTpro-labelling of N-termini and lysines were set as static modifications. False discovery rates were controlled using Percolator (<1% FDR on PSM level). Only proteins with high and medium confidence (combined q-value <0.05) were used for downstream analyses.

Mass spectrometry data analyses

For processing and statistical analysis of the MS data, the Perseus software (v. 1.6.15.0) and Microsoft Excel were used. After the removal of contaminants and reverse entries, replicates were grouped. In immunoprecipitations, proteins not identified in at least 2 replicates within one group were removed. LFQ intensities (IP samples) and normalized abundances (proteome) were log2 transformed, and missing values in IP samples were replaced by imputation using standard distribution. If not stated otherwise, a two-tailed Student's t-test was performed applying a Benjamini Hochberg FDR of 0.05. A one-tailed (right) Student's t-test with a Benjamini Hochberg FDR of 0.05 was used to compare the IP samples with the non-transfected MOCK control.

Gene ontology (GO) term enrichment analyses versus the human proteome were done using the DAVID online tool.[64] If not stated otherwise proteins were filtered with a significance level of $p < 0.05$. Proteins from IP samples were first filtered for log2FC > 0.58 over the non-transfected MOCK control in either the Control-KD, NPM1-KD, or both and defined as "real interactors". Then log2FC>+/−0.58 between the NPM1-KD and Contr-KD were used to identify interactors enriched or lost upon NPM1 depletion. Proteins from the proteomes were considered upregulated or downregulated with an FC > +/−0.2 with a significance level of $p < 0.05$.

The principal component analysis was created in Perseus. GO-term enrichment and volcano blots were created with R studio.

Proximity ligation assay and confocal microscopy

U-2 OS cells expressing doxycycline-inducible Flag-NPM1 variants were depleted of endogenous NPM1 with a UTR-specific NPM1 siRNA and grown on coverslips (0.17 mm thick, Carl Roth). If indicated, cells were treated with 200 nM Bafilomycin A1 and/or 150 nM Torin 1 for 4 h. The cells were fixed in 4% paraformaldehyde (PFA) for 15 min and permeabilized with 0.5% Triton X-100 in PBS for 10 min. The proximity Ligation Assay was performed with the Duolink system (Sigma) according to the manufacturer's instructions, if not stated differently. To reduce the background signal, the primary antibodies were diluted in PLA blocking buffer instead of the antibody dilution buffer. In the last washing step of the protocol, DAPI and fluorescently labeled secondary antibodies were added to wash buffer B for 30 min. The coverslips were mounted on a glass slide with ProLong Gold Antifade Mountant (Thermo Fisher Scientific) and dried before imaging with the Leica SP8 confocal microscope. Image processing and analysis were done with the BioVoxxel toolbox in ImageJ and the CellProfiler 4.2.1 software. Statistics was calculated in GraphPad Prism 5 for Mac OS X.

Yokogawa CQ1 microscopy imaging

U-2 $OS^{GFP-mCherry-LC3B}$ cells with doxycycline-inducible Flag-NPM1 variants or siRNA-mediated gene depletion were grown on confocal microscopy compatible μclear microplates (Greiner). If stated, cells were treated with 100 nM Bafilomycin A1 overnight, prior to the fixation. Cells were fixed with 4% PFA for 15 min, permeabilized with 0.5% Triton in PBS, and stained with Hoechst 33342 (Thermo Scientific) and Alexa Fluor 647 Phalloidin for 20 min. Imaging with the Yokogawa CQ1 microscope and analysis with the CQ1 software was performed as described previously.[86] In brief, cells were automatically detected using nuclear DAPI staining and cytoplasmic background staining. Peaks of fluorescent intensity compared to the surrounding were counted as dots. To quantify the colocalizing dots, the dots in the mCherry and GFP channels were overlayed and counted.

Lysotracker staining and live cell microscopy

U-2 OS cells, expressing doxycycline-inducible Flag-NPM1 variant or subjected to siRNA-mediated gene depletion were grown on confocal microscopy compatible μclear microplates (Greiner) and stained with 75 nM LysoTracker red DND 99 (Invitrogen) and Hoechst 33342 (Thermo Scientific) for 20 min. As described above, imaging and analysis were performed with the Yokogawa CQ1 microscope and CQ1 software. Not more than 10 wells were stained and imaged simultaneously to minimize potential cytotoxic effects.

Flow cytometry analysis

U-2 $OS^{GFP-LC3B-RFP-LC3B\Delta G}$ cells with doxycycline-inducible Flag-NPM1 variants or siRNA-mediated gene depletion were used for flow cytometry FACS Canto II and analyzed using BD FACSDiva 8.0.1 software as described.[86] If stated, cells were treated with Bafilomycin A1 or Torin 1. For statistical analysis with FlowJo, the percentage of cells in the autophagy-positive gate was used as shown by Hertel et al.[58]

Modeling and simulations of protein complexes

We modeled the 3D structure of the human NPM1-GABARAPl1 complex using AlphaFold,[62] a state-of-the-art neural network-based structure prediction method. We used a poly glycine linker (40 residues) to stitch the NPM1 and the GABARAPL1 sequence into a single polypeptide chain in both orientations (NPM1-G40-GABARAPL1 and GABARAPL1-G40-NPM1) to obtain initial models, which were then processed to remove the glycine linker to construct 10 high-resolution structural models of the binary complex.

All-atom molecular dynamics simulations of the NPM1-GABARAPL1 complexes were performed using GROMACS (version 2021.5; https://doi.org/10.5281/zenodo.10017699)[66–68] with CHARMM36m forcefield.[87] Four initial models were selected from the top-ranked AF models (Models 1, 3, 5, & 8) and processed using CHARMM-GUI.[88] Initial models were first energy minimized in vacuum, then inserted into an octahedron box (give box size), and solvated with TIP3P water and 150 mM NaCl. Following this, another round of energy minimization was executed using the steepest descent algorithm, and two separate equilibration runs (10 ns each) with positional restraints on the protein backbone atoms. The first equilibration run was performed by maintaining the temperature at 310 K using a Nose-Hoover thermostat.[89–91] In the second equilibration run, the pressure was maintained at 1 atm using the isotropic Parrinello-Rahman barostat.[92] Production runs were performed with 2 fs time steps for a total of 500 ns for the four replicates.

WT complex (GABARAPL1–$NPM1_{WT}^{1-20}$) containing the N-terminal peptide of $NPM1^{1-20}$ and GABARAPL1 (GABARAPL1) was modeled by truncating the NPM1 protein structure from the top- AF complex model. Models for mutant complexes containing the alanine mutations (GABARAPL1–$NPM1_{5A}^{1-20}$), phospho-mimics (GABARAPL1–$NPM1_{2E}^{1-20}$), and the acetylation-mimics ($GABARAPL1_{2Q}$–$NPM1_{WT}^{1-20}$) were obtained by using mutate module of CHARMM-GUI.[88] Three replicates for each complex were simulated using CHARMM36M forcefield in GROMACS employing the same protocol mentioned above for 500 ns.

Interface mapping, contact maps, and comparisons

The complex interface and the interacting residues were mapped by quantifying residue-wise inter-chain (A and B) contacts and averaged over the contact maps. Residue-wise contacts were computed using in-house scripts, using MDAnalysis[72] $AB_{cnts} = [\sum_{i \in A}\sum_{j \in B}\sigma(|r_{ij}|)]$, where the sums extend over heavy atom positions of interacting residues (i, j) and $\sigma(|r_{ij}|) = 1-(0.5+0.5\tanh(|r_{ij}|-6))$, a smooth sigmoidal counting function to limit interactions below the cut-off distance ($r_{ij} \leq 6$ Å). Contact maps were averaged over all 10 AF models to obtain interacting sites on NPM1 and ATG8 proteins. Contacts maps were also averaged over individual frames of MD trajectories (1 ns intervals for 500 ns) of the bound state of the complex. Only the bound states ($\sum AB_{cnts} \geq 5$) were averaged to obtain the contact probabilities and mapped onto the 3D structure.

QUANTIFICATION AND STATISTICAL ANALYSIS

Quantification of the data is described in the method section of the respective experiment. Statistical tests of mass spectrometry data were performed using Perseus. Statistical tests of other experimental data were performed using GraphPad Prism, version 5.0b for MAC OS X. Data were analyzed by *t* test or one-way ANOVA as indicated in the figure legends. n numbers represent biological replicates and are indicated in figure legends. Error bars indicate the standard deviation (SD) or standard error of the mean (SEM). p values are indicated as follows: * = < 0.05, ** = < 0.01, *** = < 0.001.